POLITECNICO DI TORINO
Repository ISTITUZIONALE

Rough surfaces with enhanced heat transfer for electronics cooling by direct metal laser sintering

(Article begins on next page)

05 May 2024

Rough surfaces with enhanced heat transfer for electronics cooling by direct metal laser sintering

Luigi Ventola[a], Francesco Robotti[a], Masoud Dialameh[a], Flaviana Calignano[b], Diego Manfredi[b], Eliodoro Chiavazzo[a], Pietro Asinari[a,*]

[a]*multi-Scale ModeLing Laboratory (SMaLL), Energy Department, Politecnico di Torino, Corso Duca degli Abruzzi 24, 10129 Torino, Italy*
[b]*Center for Space Human Robotics IIT@Polito, Istituto Italiano di Tecnologia, Corso Trento 21, 10129 Torino, Italy*

Abstract

Experimental evidences are reported on the potential of direct metal laser sintering (DMLS) in manufacturing flat and finned heat sinks with a remarkably enhanced convective heat transfer coefficient, taking advantage of artificial roughness in fully turbulent regime. To the best of our knowledge, this is the first study where artificial roughness by DMLS is investigated in terms of such thermal performances. On rough flat surfaces, we experience a peak of 73% for the convective heat transfer enhancement (63% on average) compared to smooth surfaces. On rough (single) finned surfaces, the best performance is found to be 40% (35% on average) compared to smooth finned surface. These results refer to setups with Reynolds numbers (based on heated edge) within $3,500 \lesssim Re_L \lesssim 16,500$ (corresponding to $35,000 \lesssim Re_D \lesssim 165,000$ in terms of Reynolds number based on hydraulic diameter). Experimental data are obtained by a purposely developed sensor with maximum and mean

---

*corresponding author:
  Email address: `pietro.asinari@polito.it` (Pietro Asinari)
  URL: `http://www.polito.it/small` (Pietro Asinari)

estimated tolerance intervals of $\pm 7.0\%$ and $\pm 5.4\%$, respectively. Following the idea by Gioia *et al.* [Phys. Rev. Lett. 96 (2006) 044502], we propose that heat transfer close to the wall is dominated by eddies with size depending on the roughness dimensions and the viscous (Kolmogórov) length scale. An excellent agreement between the experimental data and the proposed analytical model is finally demonstrated.

Nomenclature

A	flat surface area $[m^2]$
A_f	total effective surface area $[m^2]$
A_{ff}	finned surface area $[m^2]$
A_{fb}	base surface area $[m^2]$
D	hydraulic diameter $[m]$
E	heat transfer enhancement $[-]$
f	friction factor $[-]$ or probability density function $[1/m]$
h	convective heat transfer coefficient $[W/m^2/K]$
h_f	average convective heat transfer coefficient for finned surface $[W/m^2/K]$
h_d	hatching distance $[mm]$
k	core-to-guard thermal transmittance $[W/K]$; slicing direction $[-]$
k_a	average surface roughness w.r.t. fluid-dynamic plane $[\mu m]$
k_p	peak surface roughness w.r.t. fluid-dynamic plane $[\mu m]$
k_s	grain size diameter $[\mu m]$
k_0	tunable shifting parameter $[\mu m]$
L	heating edge $[m]$
l	fin length $[mm]$
m	wave number $[mm^{-1}]$
n	number of measurements $[-]$; direction normal to a sample face $[-]$
Nu	Nusselt number $[-]$
Pr	Prandtl number $[-]$
p	pressure $[Pa]$
P	probability $[-]$; laser power $[W]$
q	generic independent quantity, various units

R	hydraulic radius [μm]
R_h	heater electric resistance [Ω]
R_a	average roughness [μm]
R_p	peak roughness [μm]
R_z	five-peak-valley roughness [μm]
rs_{angle}	angle between the rough surface and the building platform [$degree$]
S	surface [m^2]
S_a	average surface roughness [μm]
S_{ku}	kurtosis surface roughness [μm]
s	minimum distance between sample temperature probe and sample surface [mm]
S_p	peak surface roughness [μm]
S_q	root mean square surface roughness [μm]
S_{sk}	skewness surface roughness [μm]
Re	Reynolds number [$-$]
T	temperature [K]
t	fin thickness [mm]
V	potential difference [V]
v	fluid velocity [m/s]; scan speed [mm/s]
y_0	friction length [μm]
z	height w.r.t. fluid-dynamic plane μm
z_d	roughness displacement μm
z_0	aerodynamic roughness length μm

Greek symbols

α significant level $[-]$

γ energetic range of turbulence spectrum $[-]$

δ size of the Kolmogórov smallest eddies $[-]$

ϵ emissivity $[-]$

η viscous length scale $[\mu m]$

η_A aerothermal efficiency $[-]$

η_f fin efficiency $[-]$

ϑ angle between the normal to a sample face and the slicing direction $[degree]$

κ Von Kármán's constant $[-]$

λ thermal conductivity of air $[W/m/K]$

λ_s thermal conductivity of sample $[W/m/K]$

λ_f roughness frontal aspect ratio $[-]$

λ_p roughness plan aspect ratio $[-]$

ν kinematic viscosity $[m^2/s]$

ρ density $[kg/m^3]$

σ relative standard uncertainty $[-]$

Σ standard uncertainty, various units

σ_B Stefan-Boltzmann constant $[W/m^2/K^4]$

τ shear stress $[N/m^2]$

ϕ specific thermal flux $[W/m^2]$

ω critical value of k_s^+ for viscous sublayer $[-]$

Subscripts and superscripts

a air

A type A uncertanity

AS	almost smooth
B	Blasius or type B uncertainty
d	downstream
eff	effective
D	hydraulic diameter
F	fitting
f	finned sample
ff	fin of the finned sample
fb	base of the finned sample
g	guard (sensor)
$g1$	upstream guard (sensor)
$g2$	downstream guard (sensor)
G	Gioia *et al.*
i	index of the i-th independent quantity
L	heating edge
m	mean line/plane
N	Nikuradse
q_i	i-th independent quantity
r	rough
s	sample (sensor)
sf	solid-fluid interface
u	upstream
w	wall
$+$	turbulence dimensionless quantities

1. Introduction and motivation

Thermal management of the microprocessors used in notebook and desktop computers often relies on chip-attached or adhesively bonded extruded aluminum heat sinks, cooled by remotely located fans [1]. In particular, battery power limitations in notebook computers represent a motivation to keep searching for heat sinks with enhanced performances. Highly efficient heat sinks, with reduced thermal resistances, are required also by high-end commercial workstations and servers. Many details about the thermal management of electronic devices and practical issues associated with the efficient packaging are reported in Refs. [2, 3]. Even though water-based two-phase cooling systems are known to ensure remarkably high heat fluxes (two- or three orders of magnitude higher than forced air systems), it is difficult to imagine a widespread use of such a technology in notebook computers, which will remain dominated by forced air convection cooling systems reasonably for long time. However, in the next-generation electronics devices, thermal performances of the air-cooled heat sinks must be further improved due to a steadily increasing power density, which makes the thermal management a great challenge still to be faced in the next future [4].

Forced air heat transfer enhancement has been extensively explored and many augmentation techniques have been already proposed [5], including plane fins [6, 7], pin fins [8, 9, 10], dimpled surfaces [11, 12, 13], surfaces with arrays of protrusions [14, 15], metal foams [16], and artificial surface roughness [17]. By *artificial surface roughness*, we mean any surface patterning with enough regularity and purposely designed in order to enhance heat transfer. For instance, in such a category, we may include ribs [18, 19, 20]

7

and, more recently, (shark-skin-like) scale roughened surfaces [21, 22]. The resulting heat transfer enhancement of the scale roughened surface is surprisingly good compared to rib roughened and dimpled surfaces [23]. This proves that there is still room for improving the optimal design of artificial surface roughness. To this respect, an interesting possibility consists in adopting a multi-scale strategy, where pin micro-fins are placed on standard plate fins. Recently, Authors in Ref. [24] showed that pin fins of five different cross-section shapes in channels of plate-fin heat sinks cause enhancement in the heat transfer. Short pin fins, on surfaces of plate-fin heat sinks, prove to be particularly effective, in spite of their modest thicknesses: Authors in Ref. [25] achieved a heat transfer enhancement of 78% by pin fins shorter than $350\,\mu m$. These first results seem to open the field to a *hierarchical* design of micro-structures, purposely designed in order to exploit at best the thermo-fluid dynamics boundary layers and thus achieve the highest heat transfer coefficient. Another interesting possibility consists in using ionic wind engines, which can be integrated onto surfaces to provide enhanced local cooling [26]. Air ions generated by field-emitted electrons or corona discharges are pulled by an electric field and exchange momentum with neutral air molecules, causing air flow [26]. Beyond pin micro-fins, sharp electrodes by wires can also be adopted [27].

Micro-fins patterning of heat sinks made by standard milling for electronics cooling may be impracticable due to technological constraints (e.g. accessibility of fin surfaces in plate fins) and/or not economically viable (because it would require an additional post-processing in manufacturing). On the other hand, additive manufacturing (AM) technologies represent an in-

teresting alternative.

The ability to modify a design and to create immediately the component designed, without wasteful casting or drilling, makes additive manufacturing an economical way to fabricate single items, small batches, and, potentially, mass-produced items. Large aerospace companies, such as Boeing, GE Aviation, and Airbus, are working hard on qualifying AM processes and materials for flight. Boeing, for example, now has 200 different AM part numbers on 10 production platforms, including both military and commercial jets. Many events conducted by industry, academia, and government have presented examples of how the technology is being applied to the production of parts for products. Most involve relatively small volumes of parts, such as tens or hundreds for the aerospace, medical, and jewelry industries. Two exceptions are the manufacture of custom-fit, in-the-ear hearing aids and dental copings for crowns and bridges. Millions of hearing aids and dental copings are being produced annually. Each product is unique in shape and size, and that is where AM excels [28]. GE Aviation also plans to use AM to produce the titanium leading edges for the LEAP engines fan blades. Meanwhile, German company EOS GmbH, a leading manufacturer of metal powder bed fusion systems, estimates that 15,000 dental copings are made in the companys machines every day [29].

Thanks to these manufacturing techniques (often referred to as layer manufacturing or rapid prototyping), it is possible to build highly complex components from a three-dimensional computer-aided design (CAD) model without part-specific tooling [30]. Selective Laser Melting (SLM) is an AM process where a laser source selectively scans a powder bed according to

the CAD-data of the part to be produced. The high intensity laser beam makes it possible to completely melt and fuse the metal powder particles together to obtain almost fully dense parts. Successive layers of metal powder particles are melted and consolidated on top of each other resulting in near-net-shaped parts [30]. Research in recent years has identified the potential of this process to build metallic components that can act as functional prototypes. The ability of SLM to produce complex three-dimensional structures with features that would be difficult if not impossible to manufacture using conventional methods has been already explored for building heat sinks [31], as well as miniature heat exchangers and radiators [32]. Moreover, with the proper choice of input conditions, direct metal laser sintering (DMLS, the trade name by EOS GmbH for SLM) can build full dense parts with mechanical properties equivalent or even superior to those of parts produced by conventional manufacturing [33, 34]. Moreover, the surface morphology of these parts can also be tuned (to some extent), in order to produce artificial roughness with some desired features.

In this paper, for the first time to our knowledge, we experimentally investigate the potential of the DMLS artificial roughness, optimized for convective heat transfer enhancement, in manufacturing flat and finned heat sinks for electronics cooling. This is different from previous works [31, 32], which focused on the flexibility in manufacturing complex designs, neglecting further opportunities due to artificial roughness.

The paper is organized as follow. In Section 2, experimental data are reported and discussed, including some details about direct metal laser sintering, morphological and radiative characterization of rough surfaces and

10

convective heat transfer equipment. In Section 3, the theoretical models are presented and discussed, including sand-based models, canopy-based models and the proposed model. Finally, in Section 4, conclusions are drawn and perspectives are discussed.

2. EXPERIMENTAL DATA

2.1. Rough surfaces by direct metal laser sintering (DMLS)

Current state-of-the-art DMLS techniques allow one to produce bulk object without significant porosity. Using optimized process parameters is possible to obtain a residual porosity below 0.8% [34]. Due to its versatility in terms of both materials and shapes, the main advantage of DMLS is to produce metal complex-shaped components in one step. In the present study, all samples are made of AlSiMg alloy supplied by EOS GmbH. The above alloy comes as a powder, whose element shape, dimensions, size distribution (with volume assumption), chemical composition and percentage in weight were assessed in a previous work [34]. The aluminum alloy specimens were prepared by DMLS with an EOSINT M270 Xtended version. In this machine, a powerful Yb (Ytterbium) fiber laser system in an Argon atmosphere is used to melt powders with a continuous power up to 200 W.

DMLS process starts with the creation of a three-dimensional CAD-model of an object. Then the model is converted to a STL file format. This file defines optimal building direction of the physical object and it is based on small triangles, which determine the accuracy and contours of the whole object. Then, the support structures are generated and subsequently, together with the STL model, are sliced into horizontal layer of 30 μm thickness.

These SLI format files are then transferred to the computer of the DMLS machine, which now has the necessary information to build up each layer. The essential operation in the DMLS process is the laser beam scanning over the surface of a thin powder layer previously deposited on a substrate. The forming process goes along the scanning direction of the laser beam. Each cross-section (layer) of the part is sequentially filled with elongated lines (vectors) of molten powder. The quality of a part produced by this technology depends strongly on the quality of each single vector and each single layer. Identification of the optimal process parameters of laser power, scanning speed and hatching distance is a crucial task because these parameters happen to be the most influential on the parts characteristics: surface quality, porosity, hardness and mechanical properties [35].

Accuracy and part surface quality has become the focus of AM community with the increased requirement of prototyped functional parts, enhanced material properties for strength and dimensional tolerance comparable to conventionally producible parts. Since the whole object is manufactured starting from tessellation of a 3D CAD model, the contour of a DMLS part is a stepped approximation of the contour of the nominal CAD model. As a result of this, all parts manufactured by AM processes exhibit a staircase effect. The uniform slicing procedure directly affects the extent of the staircase effect that appears especially along inclined planes and curved surfaces. As the inclination angle is reduced or the layer thickness is increased, the stair-effect becomes more pronounced. When the slicing thickness is thinner, the staircase is smaller and the surface will be smoother. The error associated with the staircase effect can be quantified by considering the cusp height
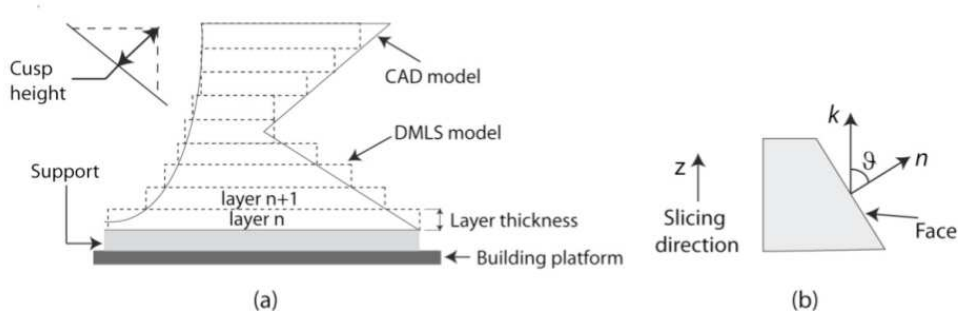
Figure 1: (a) Staircase effect on the DMLS model; (b) Building orientation.

in Figure 1(a) which is the maximum distance between the nominal part boundary and the boundary of the part produced by DMLS. In any building orientation, the part is defined with its base on the xy-plane, the building direction along the z axis and the angle ϑ defined as the angle between the vector normal to the face (n) and the slicing direction (k) - see Figure 1(b). When the intersection angle ϑ is equal to or less than the critical value, the region needs adding support. The need to improve the surface finish of the parts produced by DMLS has led to a variety of researches on reducing of the staircase effect on inclined and curved surfaces and on the choice of the process parameters. In this study, starting from the results obtained previously on the optimization of process parameters on surface finish of AlSiMg sample produced by DMLS [35], values which can modify and increase the surface roughness were chosen. Samples dimension were $11.1 \times 11.1 \times 5$ mm and they were orientated with angles from 90 to 0. The parts with angles from 40 to 30 show a higher surface roughness due to the staircase effect.

However, a higher surface roughness should not be detrimental concerning the residual sub-surface porosity, otherwise the heat transfer performance

13

Table 1: Thermal properties of parts [36]. Heat treatment (last column) by annealing process for 2 h at 573 K for stress relieve.

	As built	Heat treated
Thermal conductivity, λ_s		
- in horizontal direction	$103 \pm 5 \; W/m/K$	$173 \pm 10 \; W/m/K$
- in vertical direction	$119 \pm 5 \; W/m/K$	$175 \pm 10 \; W/m/K$
Specific heat capacity		
- in horizontal direction	$920 \pm 50 \; J/kg/K$	$890 \pm 50 \; J/kg/K$
- in vertical direction	$910 \pm 50 \; J/kg/K$	$900 \pm 50 \; J/kg/K$

may be negatively affected. To avoid such effect, the laser speed on the surface and sub-surface region must be kept as constant as possible. This is not trivial because during scanning a certain time is needed to accelerate the mirrors to the desired speed. This is due to inertia of mirrors used for scanning. During this time, the laser beam moves at a non constant speed: hence more energy is applied at the edges of the part than in the bulk. To avoid this situation, the mirror is accelerated already before the start of the part so that it has reached the desired speed before the beginning of exposure (skywriting option in EOS GmbH technology). This strategy proved to be effective for building the present samples with extremely low porosity (see Fig. 5). Low porosity ensures very good thermal properties of parts, which can be improved even further by heat treatment, as shown in Table 1.

After being manufactured and removed from the building platform, five parallelepiped facets are milled in order to fit into the convective heat sensor (see next section and Fig. 7). The remaining sample facet maintains the
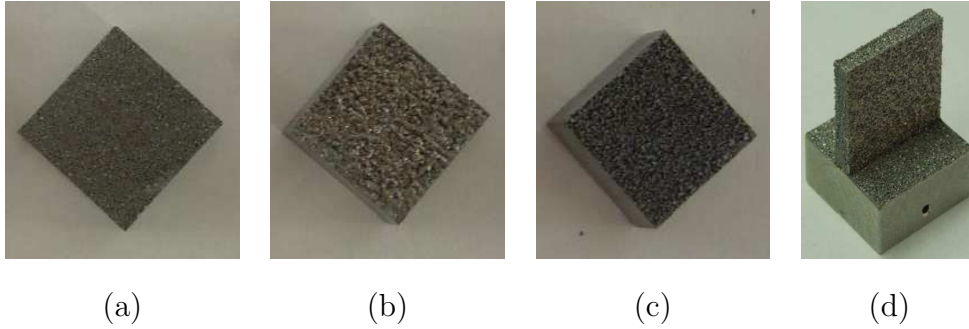
14

(a)   (b)   (c)   (d)

Figure 2: Tested samples made of AlSiMg alloy by direct metal laser sintering (DMLS): (a) sample #1, average roughness $R_a = 16\ \mu m$; (b) sample #2, $R_a = 24\ \mu m$; (c) sample #3, $R_a = 43\ \mu m$; (d) sample #4, finned surface, roughly $R_a = 22\ \mu m$ as average on both sides.
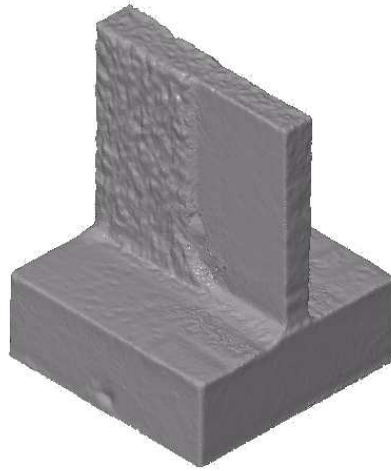

Figure 3: Example of 3D optical scan of sample #5 made by milling both horizontal surfaces and fin half sides, after testing sample #4. The other physical dimensions remain the same.
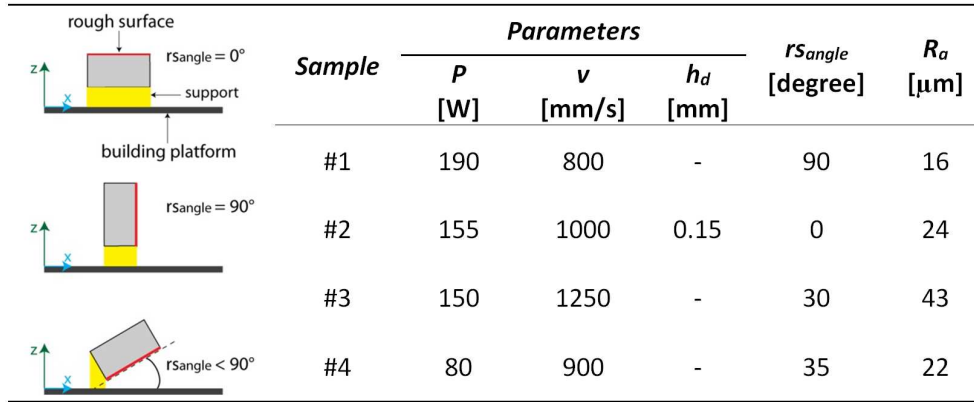
	Sample	Parameters			rs_{angle} [degree]	R_a [μm]
		P [W]	v [mm/s]	h_d [mm]		
	#1	190	800	-	90	16
	#2	155	1000	0.15	0	24
	#3	150	1250	-	30	43
	#4	80	900	-	35	22

Figure 4: Process parameters and orientation in the building platform of the samples produced by DMLS (P=laser power, v= scan speed, h_d=hatching distance [35]).

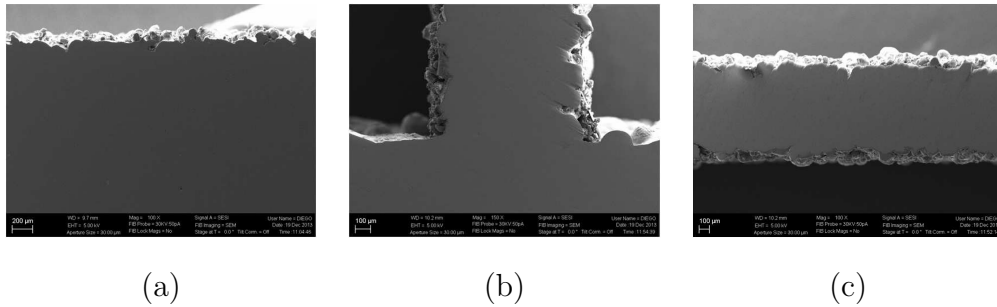(a)   (b)   (c)

Figure 5: Characterization of the residual porosity of the DMLS samples by Field Emission Scanning Electron Microscopy (FESEM): No sub-surface porosity is visible. (a) sample #1; (b) sample #4, fin root; (c) sample #4, finned surface, fin middle.

original roughness due to the DMLS manufacturing and it will be named rough surface in the following description. The first three samples are characterized by flat rough surfaces, see subplots (a, b, c) in Fig. 2. In the fourth sample, see subplot (d) in Fig. 2, the rough surface has an additional orthogonal fin of size $11.1 \times 10 \times 2 \ mm$, in order to explore finned surfaces as well. Finally, the fifth sample, see Fig. 3, is obtained by milling both horizontal surfaces and fin half sides of the fourth sample. For convenience, the tested samples (reported in Fig. 2) are identified by the standard average roughness R_a. However, a more sophisticated surface characterization (with respect to R_a) will be discussed in the following section. Those samples were obtained by varying the angle between the rough surface and the hatching DMLS plane in order to explore the impact of this parameter on the surface morphology and consequently on the thermal performances. Figure 4 shows the angle of construction of the samples, the process parameters used for rough surface and the average roughness obtained. The angle considered was the one comprised between the rough surface and building platform (rs_{angle}). The considered samples have extremely low porosity (see Fig. 5). Heat treatment has been applied to all tested samples, in order to improve further their thermal properties (see Table 1 for details). Smooth samples (both in aluminum and copper) made by milling with $R_a \approx 1 \ \mu m$ were also used as a reference. The latter roughness value is typical of heat dissipators for electronics, which are usually obtained by traditional milling, and hence it is particularly suitable for estimating the relative thermal enhancement.
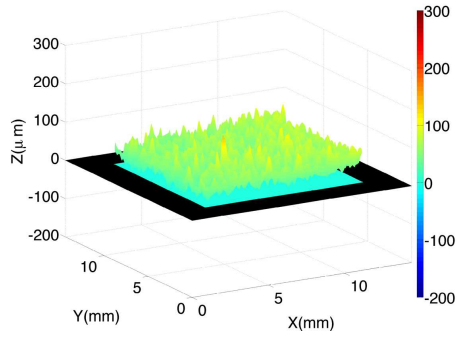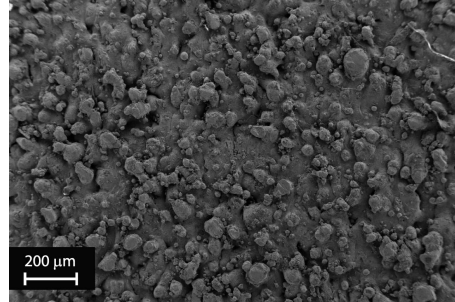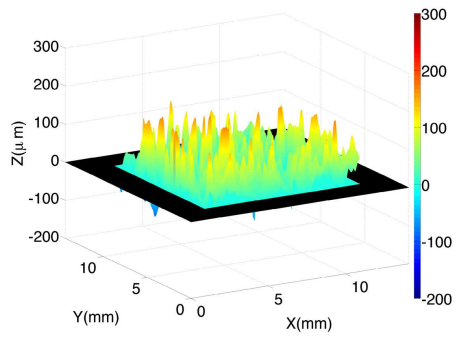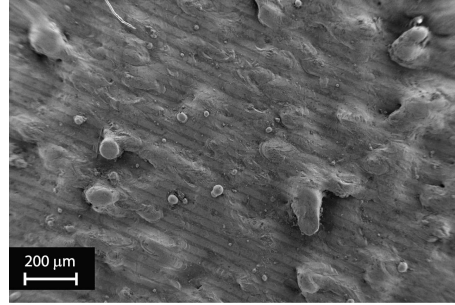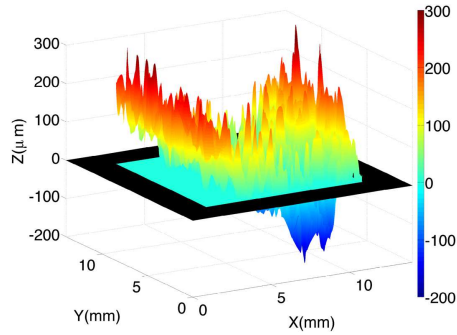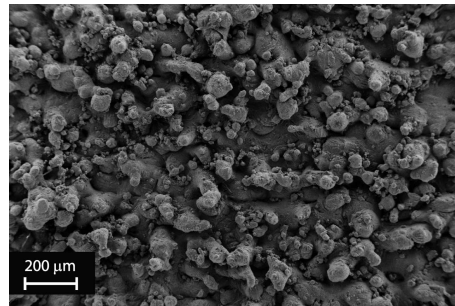
Figure 6: Surface morphological characterization of flat samples: (a, c, e) by 3D optical scanner referring to the fluid-dynamic plane and (b, d, f) by Field Emission Scanning Electron Microscope; (a, b) sample #1, $R_a = 16\ \mu m$; (c, d) sample #2, $R_a = 24\ \mu m$; (e, f) sample #3, $R_a = 43\ \mu m$.

18

2.2. Morphological and radiative characterization of rough surfaces

In this section, a detailed morphological analysis is reported for the tested samples shown in Fig. 2. First of all, the samples were characterized by a 3D optical scanner ATOS Compact Scan 2M (GOM GmbH) with the results reported in the subplots (a, c, e) of Fig. 6. The latter figures reveal a complex multi-scale morphology (at least for samples #1 and #3), which could be ascribed to the contour parameters used together with the powder adopted. In fact the mean particle diameter ranges from 0.5 to 40 μm, but the small particles are far more (in number) than the bigger ones, thus creating clusters with complex morphology at the micro-metric scale. On the other hand, in sample #2, as described in the previous paragraph, the rough surface was parallel to the hatching plane, so associated to different building parameters, and this allows the free metal surface (due to laser melting) to smooth out more homogeneously. We notice that the FESEM images are reported by planar view, thus it is not simple to estimate therein the actual height of the peaks.

In order to make more quantitative analysis, let us introduce the so-called *R-parameters* [37] and the *S-parameters* [38]. First, the arithmetic average height parameter R_a is defined as

$$R_a = \frac{1}{n} \sum_{i=1}^{n} |z_i - z_m|, \tag{1}$$

where z_i is the height of the generic rough surface point i-th with respect to the fluid dynamic reference plane (see next), $z_m = z_m(s)$ is the least squares mean line of the rough profile (not necessarily constant), s is the generalized coordinate of the profile and n is the number of profile points measured by

a rugosimeter. Clearly, the above definition holds under the assumption of homogeneously distributed profile points, as usually occurs in this kind of measurements. Another popular *R-parameter* is given by R_z, which is the difference in height between the average of the five highest peaks and the five lowest valleys along the assessment length of the profile. This value is usually larger than R_p, which is the maximum height of the linear profile.

Previous parameters have the limitation of referring to a specific profile measured by the rugosimeter and they may lead to inaccurate estimates for the whole surface. Hence the *S-parameters* [38] have been proposed. The arithmetical mean height of the surface S_a has a definition very similar to Eq. (1), but now z_m is the least squares mean plane of the rough profile, namely $z_m = z_m(s_1, s_2)$, where s_1 and s_2 are the two planar generalized coordinates. Similarly, S_p is the maximum height of the peak and S_q is the root mean square height of the surface. Moreover, high order moments are also commonly used. For example, the skewness S_{sk} (third order moment) and the kurtosis S_{ku} (fourth order moment). The sign of S_{sk} indicates the predominance of peaks (i.e. $S_{sk} > 0$) or valley structures ($S_{sk} < 0$) on the surface as compared to a Gaussian distribution ($S_{sk} = 0$). On the other hand, S_{ku} indicates the presence of inordinately high peaks/deep valleys ($S_{ku} > 3$) or lack thereof ($S_{ku} < 3$) making up the texture with respect to a Gaussian distribution ($S_{ku} = 3$). More details can be found in Ref. [38].

Samples in Fig. 2 were characterized in terms of the *R-parameters* using a RTP80 instrument (SM instruments) for roughness measurements. On the other hand, the *S-parameters* were computed by applying the standard definitions [38] to the three-dimensional profiles obtained by the optical scanner

Table 2: Morphological statistical moments of tested samples (see Fig. 2): *R-parameters* (R_z and average R_a); *S-parameters* (maximum S_p, average S_a, root mean square S_q, kurtosis S_{ku} and skewness S_{sk}) and *k-parameters* (maximum k_p and average k_a). For sample #4, left and right denote the corresponding sides of the fin. A_r is the roughness surface area and A is the reference planar area. The *k-parameters* were obtained by averaging five mechanical mountings on the proposed sensor.

Sample	R_z	R_a	S_p	S_a	S_q	S_{ku}	S_{sk}	A_r/A	k_p	k_a	$\lambda_p = k_a/k_p$
	$[\mu m]$	$[\mu m]$	$[\mu m]$	$[\mu m]$	$[\mu m]$			$[\%]$	$[\mu m]$	$[\mu m]$	
#1	79.1	15.8	41	12	15	3.01	0.31	1.1	185	83	0.45
#2	132.6	23.5	89	27	34	2.88	0.32	3.4	248	96	0.38
#3	237.8	43.0	118	36	45	2.78	0.32	6.9	378	112	0.30
#4 (left)	99.5	20.6	38	15	18	2.89	-0.21	-	-	-	-
#4 (right)	108.8	23.9	67	25	31	2.59	0.12	-	-	-	-

Table 3: Estimated emissivity of tested samples (see Fig. 2): Al refer to milled smooth samples ($R_a \approx 1\ \mu m$) used as reference for computing heat transfer enhancement.

Sample (see Fig. 2)	R_a [μm]	Real [℃]	Estimated [℃]	ϵ
Al	1	50.5	50.8	0.10
#1	16	55.5	55.6	0.35
#2	24	52.5	52.0	0.20
#3	43	43.9	43.0	0.39

(where, in order to apply the previous definitions, an interpolated homogeneous mesh was adopted). All results are reported in Table 2. The tested sample surfaces show a peak distribution close to a Gaussian, i.e. $S_{ku} \approx 3$ and $S_{sk} \approx 0$. More importantly, the flat surfaces reveal $S_a/S_p \approx 0.3$, while both sides of the fin have $S_a/S_p \approx 0.4$.

It is well known that roughness can influence the surface emissivity and consequently radiative heat transfer. Since the present study focuses on convective heat transfer only, the contribution due to radiative heat transfer is removed by post-processing the experimental data. To this end, emissivity of surfaces is estimated as described below. In order to minimize the spurious optical effects due to the surrounding environment, all samples were first placed in a dark room, and subsequently heated up with their real temperature measured by a thermocouple (in direct contact with the sample). At the same time, the sample temperature was estimated by an infrared thermal imaging camera (NEC TH9100 Series). The latter camera provides an estimated temperature after setting the surface emissivity which, in this case,

was regarded as a tunable parameter. The surface emissivity of the camera was tuned such that the estimated value was as close as possible to the real value (mismatch < 1 K). The results are reported in Table 3. As expected, these data clearly show that the rough samples present higher emissivity compared to the smooth one, although no evident relationship between the emissivity ϵ and the average roughness R_a was found. The higher emissivities of sample #1 and #3 might be explained by the multi-scale morphology, already pointed out by the FESEM analysis (see Fig. 6).

2.3. Convective heat transfer equipment and experimental procedure

The convective heat transfer through the rough facet of all samples (Fig. 2) was measured by a purposely developed sensor [39]. The key-idea is to use the notion of thermal guard for measuring the convective heat transfer coefficient. Guarded hot plate method [40] has been extensively used in measuring thermal conductivity. However, the ability of the guard to prevent undesired heat flows can be conveniently used for measuring convective heat transfer coefficients as well. In fact, the US National Institute of Standards and Technology (NIST) has developed a convective heat flux facility to allow calibration of heat flux sensors based on a guarded calibration plate [41]. An isometric view and a cross-sectional diagram of the proposed sensor are reported in subplots (a) and (b) of Fig. 7, respectively. The present sensor is made of three essential parts: (a) sample, (b) insulation shield and (c) guard. A heater is placed at the bottom of the sample, with the latter made of highly conductive material because it is devoted to efficiently transfer heat towards the flushing flow. The sensor consists of an onion-like structure: the insulation shield, made of a poorly conductive material, wraps the sample,
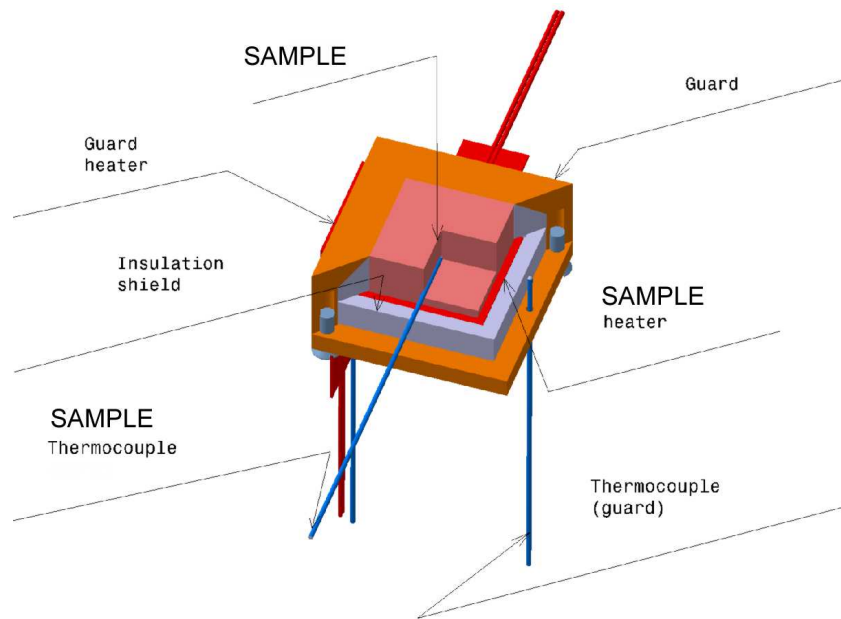
(a)
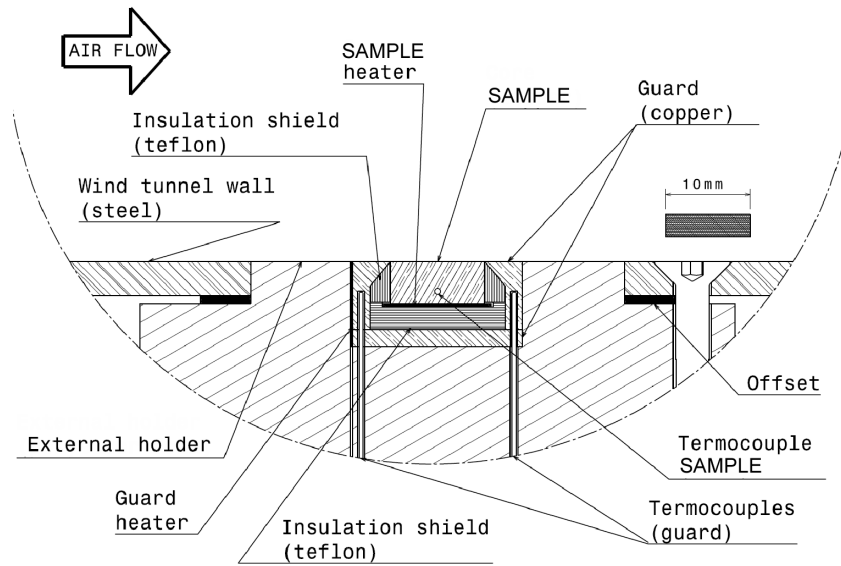
(b)

Figure 7: Purposely developed novel sensor for measuring convective heat transfer through rough surfaces [39]: (a) Isometric view (color on-line); (b) Cross-sectional diagram.

24

while a highly conductive guard wraps the assembly consisting of both the sample and the insulation shield. The insulation shield and the guard are accurately manufactured such that the guard sharply joins the sample, letting the insulation shield be in contact with the air stream only along a very narrow edge (ideally with zero area), while the top sensor surface (belonging to both the guard and the sample) is exposed to the flow and appears as a unique element.

As a result, we obtain two independent thermal circuits, where the sample heater generates the thermal power to be removed by the tested surface, while an auxiliary heater provides the thermal energy to the guard until isothermal condition is reached (i.e. negligible conduction heat transfer between the guard and the sample).

A numerical model using the fluid dynamic software Fluent™ [42] has been adopted for both numerically test the above idea and design the sensor prototype. Details on this sensor model will be reported elsewhere.

Ideally, the balance is reached when both the rough surface and the guard are at the same temperature. In practice, in our experiments, the balance condition is considered fulfilled when the sample temperature T_s (measured at the sample center) matches an averaged guard temperature $T_g = (T_{g1} + T_{g2})/2$, measured in the guard upstream (T_{g1}) and downstream (T_{g2}) walls, up to a certain precision (see also Fig. 7). Let us suppose in the model that $T_s - T_g = 0.2$ K, and consequently that part of the power provided by the sample heater flows towards the guard. The above numerical model was used to compute that, in case of a guard made of copper, the power lost towards the guard is 4 % of the total sample heater power. The model enables to

25

express (using linear extrapolation) the conduction losses towards the guard as $k\,(T_s - T_g)$, where the parameter k needs to be estimated once for all, and it depends on the sensor geometry and materials. In our setup, we found that $k = 0.01\ W/K$. Moreover, based on the above numerical model, we found that at a maximum temperature difference on the sensor surface of $(T_s - T_g)_{max} = 0.3\ K$ corresponds a difference of $0.2\ K$ in the measured temperatures.

For simplicity, let us start with flat samples. For computing the average convective heat transfer coefficient at the flat sample surface, we use the the following equation

$$h = \frac{V^2/R_h - \epsilon\,\sigma_B A(T_s^4 - T_w^4) - k\,[T_s - (T_{g1} + T_{g2})/2]}{A(T_s - T_a)}, \qquad (2)$$

where V and R_h are the potential difference across the sample heater resistance and the value of its electrical resistance, respectively, $\sigma_B = 5.67 \times 10^{-8}$ $W/m^2/K^4$ is the Stefan-Boltzmann constant, ϵ is the emissivity of the sample surface, T_s is the sample temperature measured by the thermocouple inserted in the center of the sample, T_w is the temperature of the channel wall, $k = 0.01\,W/K$ is the sample-to-guard coupling transmittance, T_{g1} and T_{g2} are the temperatures measured by the (upstream and downstream) thermocouples installed into the thermal guard, $A = 1.23\ cm^2$ is the sample surface and, finally, T_a is the temperature of the flowing air. The temperature T_s is not the reference temperature at the solid-fluid interface T_{sf}, which should be considered in the measurement of the convective heat transfer coefficient. For flat samples, the difference can be estimated by heat conduction equation under steady state conditions, namely $T_s - T_{sf} = \phi\,s/\lambda_s$, where ϕ is the specific thermal flux through the sample, s is the minimum distance between the

sample temperature probe and the sample (base) convective surface (equal to 3.5 mm), and λ_s is the sample thermal conductivity. In highly thermally conductive samples, the difference between T_s and T_{sf} can be safely neglected. For example, considering the AlSiMg samples, which have the lowest thermal conductivity among the tested samples (equal to 170 ± 10 $W/m/K$, see Table 1), and a specific thermal flux equal to 1.1 kW/m^2 (the highest among all tests), the maximum temperature difference becomes 0.02 K, which is smaller than the standard uncertainty of the calibrated thermocouple.

In the case of finned samples, the previous Eq. (2) must be easily generalized. The average convective heat transfer coefficient of finned sample surface is computed by:

$$h_f = \frac{V^2/R_h - \epsilon\,\sigma_B A_f (T_{sf}^4 - T_w^4) - k\,[T_s - (T_{g1} + T_{g2})/2]}{A_f(T_{sf} - T_a)}, \qquad (3)$$

and

$$T_{sf} = T_s - \frac{s\,V^2}{\lambda_s A R_h}, \qquad (4)$$

where A_f is now the total effective surface, namely $A_f = \eta_f A_{ff} + A_{fb}$, A_{ff} is the area of all fin sides, η_f is the fin efficiency, A_{fb} is the base surface area (for sample #4, $A_{ff} = 2.81$ cm^2 and $A_{fb} = 1.00$ cm^2). It is worth noting that the thermal flux generated at the bottom of the sample is dissipated through both fin sides, i.e. $\eta_f A_{ff}$, and base surface area, i.e. A_{fb}. Hence the previous convective coefficient h_f must be interpreted as an average over the whole dissipating surface A_f, such that the total convective transmittance becomes $h_f(\eta_f A_{ff} + A_{fb})$. However, this is relevant for electronics cooling, because total surface actually matters for heat sinks. The estimation of the fin efficiency is not trivial, because η_f is a function of the unknown h_f. It

can be computed by the following formula [1]

$$\eta_f = \frac{\tanh(m\,l)}{m\,l}, \tag{5}$$

where l is the fin length, m is given by

$$m = \sqrt{\frac{h_f}{\lambda_s\,(t/2)}}, \tag{6}$$

and t is the fin thickness. Equation (3) together with Eqs. (5, 6) can be solved iteratively: Starting with a first guess $\eta'_f = 1$, h'_f is computed by Eq. (3), m' by Eq. (6), η''_f by Eq. (5) and so on. However, it is easy to verify that, for the reported experiments, one iteration is enough to obtain h_f within the desired accuracy. For example, considering the AlSiMg-made rough finned sample at the highest Reynolds number, h'_f is equal to 219.33 $W/m^2/K$, $h''_f = 226.15$ $W/m^2/K$ and $h'''_f = 226.36$ $W/m^2/K$: Because $(h'''_f - h''_f)/h''_f \approx 0.1\%$ there is no need to perform the second iteration step, namely $h_f \approx h''_f$.

Let us now discuss the typical values of measured quantities and the corresponding accuracy. For the flat samples, the typical power generated by the sample heater is roughly $V^2/R_h \sim 0.13$ W. The temperature difference between the sample thermocouple and the air temperature ranges within 7.2 $K \leq T_s - T_a \leq 32.7$ K. For the finned samples, the typical power generated by the sample heater ranges within 0.36 $W \leq V^2/R_h \leq 0.53$ W, with the temperature difference between the sample and air 5.9 $K \leq T_s - T_a \leq 23.1$ K. Estimating experimental uncertainties (see Appendix A), it is possible to find out that the maximum and mean estimated relative uncertainty for all the convective heat transfer coefficients is $\pm 7.0\%$ and $\pm 5.4\%$, respectively. The same maximum experimental uncertainty of $\pm 7.0\%$ applies to the Nusselt

28

number, because we assumed fixed air properties. In the following figures, each Nusselt number value is reported with its error bar, pertinent to the considered experimental test (see Appendix A for details). It is important to highlight that these values are tolerance intervals which are larger than confidence intervals, which are instead usually reported in the literature on convective heat transfer measurements. We therefore prefer to work with more conservative estimates.

It must be stressed out that the proposed sensor is also the sample housing. The sensor is flush-mounted in a wind tunnel and hence it dictates the relative positioning of the rough surface with respect to the boundary layer. The *S-parameters* are not suitable to describe the heat transfer enhancement, because they are defined with respect to the least squares mean plane, namely $z_m = z_m(s_1, s_2)$, which is not related (in principle) with the fluid dynamic reference plane, sustaining the boundary layer. For this reason, we propose here to use *k-parameters* instead: they have similar definitions, but are defined with respect to the wind tunnel wall (i.e. the fluid dynamic reference plane). Moreover we exclude all the portion of the rough surface with $z_i < 0$ (for simplicity, dimpling effects are omitted in this work [43]). Consequently, the arithmetic average height parameter k_a is defined as

$$k_a = \frac{1}{n} \sum_{i=1}^{n} \mathcal{R}(z_i), \tag{7}$$

where $\mathcal{R}(x)$ is the ramp function, namely $\mathcal{R}(x) = x\,\mathcal{H}(x)$, and $\mathcal{H}(x)$ is the Heaviside step function ($\mathcal{R}(x) = x$ for $x \geq 0$ and zero otherwise, meaning that the ramp function allows one to take into account only positive values). Similarly, k_p is the maximum height of the peak, namely $k_p = \max(z_i)$. For

29

the first three samples, the *k-parameters* are reported in Table 2. All these values were obtained by averaging results from five mechanical mountings. The current implementation of the described sensor is not intended to achieve extremely precise housing: hence deviations on *k-parameters* are expected and the values reported in the table must be considered as approximate.

For the sake of completeness, a few more details about the equipment for measurements are reported below. The proposed sensor is designed for samples with size of $11.1 \times 11.1 \times 5\ mm$. The rough surface ($11.1 \times 11.1\ mm$) was flush-mounted in a wind tunnel (described below). The sample was heated from below by an electrical heater, here named sample heater, which is a $12.7 \times 12.7\ mm$ Minco flexible heater with a nominal resistance of 25.7 Ω. We measured independently the actual value of such resistance by high-precision multimeter (see next), its dependence on the operating temperature and we used in Eq. (2) a fitting curve for $R_h = R_h(T)$. For the temperature range used in all experimental tests, we found $25.66\,\Omega \leq R_h(T) \leq 25.73\,\Omega$. Thermal grease was used for reducing thermal resistances at all contact surfaces of the device, when appropriate. Sample are surrounded by an insulation shield made of Teflon™ . This element consists of a $16 \times 16 \times 3\ mm$ plate from the bottom and a $2.4\,mm$-thick taper ring with a sharp edge at the test surface. Finally, the assembly consisting of sample and shield is wrapped by a thermal guard made of copper. The guard heater (same as the sample heater) is positioned below the guard. Finally, the sensor assembly is held by an insulator container made of nylon, which is fixed to the wind tunnel. Three temperatures are measured in the proposed sensor, by means of Chromel-Alumel (type K) thermocouples with probe sheath diameter of $0.5\ mm$. The

first one crosses all sensor layers till the center of the sample. The remaining two thermocouples are inserted in the upstream and downstream wall, respectively (see Fig. 7). Two HQ PS3003 variable power suppliers (voltage range $0 - 30\,V$ and $0 - 3\,A$) are used to supply both the sample heater and the guard heater. The potential difference across the sample resistance is measured by Multimeter Agilent 34401A.

This sensor is installed in a small open-loop wind tunnel, consisting of a horizontal rectangular flow channel in thermal equilibrium with the environment. The channel has a smooth inner surface, with cross section of $228 \times 158\,mm$ (hydraulic diameter $D = 187\,mm$) and entrance length of $5\,m$ (corresponding to roughly 26 hydraulic diameters). Air is blown by a Savio s.r.l. centrifugal fan type SFL 25-A (maximum flow rate $70\,m^3/min$ at 420 Pa, maximum pressure difference 1900 Pa at 18 m^3/min), with a throttling valve for regulating the mass flow rate. At the end of the channel, downstream from the test section, a vane anemometer Testo 450 by Testo AG was used for measuring the axial velocity. The certificate of calibration of the anemometer provided also the maximum experimental uncertainty, namely $\pm 6.0\%$. The same maximum experimental uncertainty of $\pm 6.0\%$ applies to the Reynolds number as well, because we assumed fixed air properties. We correlate the average velocity with the measured axial velocity by a fluid dynamic numerical model, which was solved by Fluent™. The air temperature is measured at the same location where the anemometer is installed (not affected by the power released by the sensor itself). The thermocouple probe sheath is embedded in a block of polyester foam ($1 \times 1 \times 5\,cm$), covered by an aluminum foil, ensuring stable measurements and negligible effects due

to radiation. Similarly, the channel wall temperature is measured by a thermocouple installed on the outer surface of the channel, covered by a block of polyester foam (1 cm thick) with an external aluminum foil. Also in this case, Chromel-Alumel (type K) thermocouples were used.

Finally, all the adopted thermocouples and the vane anemometer were calibrated according to standards provided by ACCREDIA, the Italian National Accreditation Body appointed by the State to perform accreditation activity.

2.4. Experimental results

In this section, the experimental data and the measured heat transfer enhancements are reported for the tested samples. The experimental data about convective heat transfer (sample #1, #2 and #3 in Fig. 2) are reported in Fig. 8 in terms of the Nusselt number $Nu_L = h\,L/\lambda$, where $\lambda = 2.622 \times 10^{-2}$ $W/m/K$ for air, while $L = 2$ cm is the length of the heating edge of the proposed sensor, and the Reynolds number $Re_L = v\,L/\nu$, where $\nu = 1.544 \times 10^{-5}$ m^2/s for air and v is the (mass) average velocity in the wind tunnel. Maddox & Mudawar [44] worked with a similar setup and already realized that the heating edge is the appropriate length (more than the channel hydraulic diameter) for scaling the experimental results. The latter evidence was later confirmed in Ref. [45]. For this reason, the experimental results are presented in terms of Nu_L and Re_L. The agreement with phenomenological correlation proposed by Maddox & Mudawar [44] depends on the thermal footprint surrounding the sensor: in particular, less diffusive supports (i.e. in polyester foam) produce a better agreement with the previous correlation. On the other hand, supports made of materials
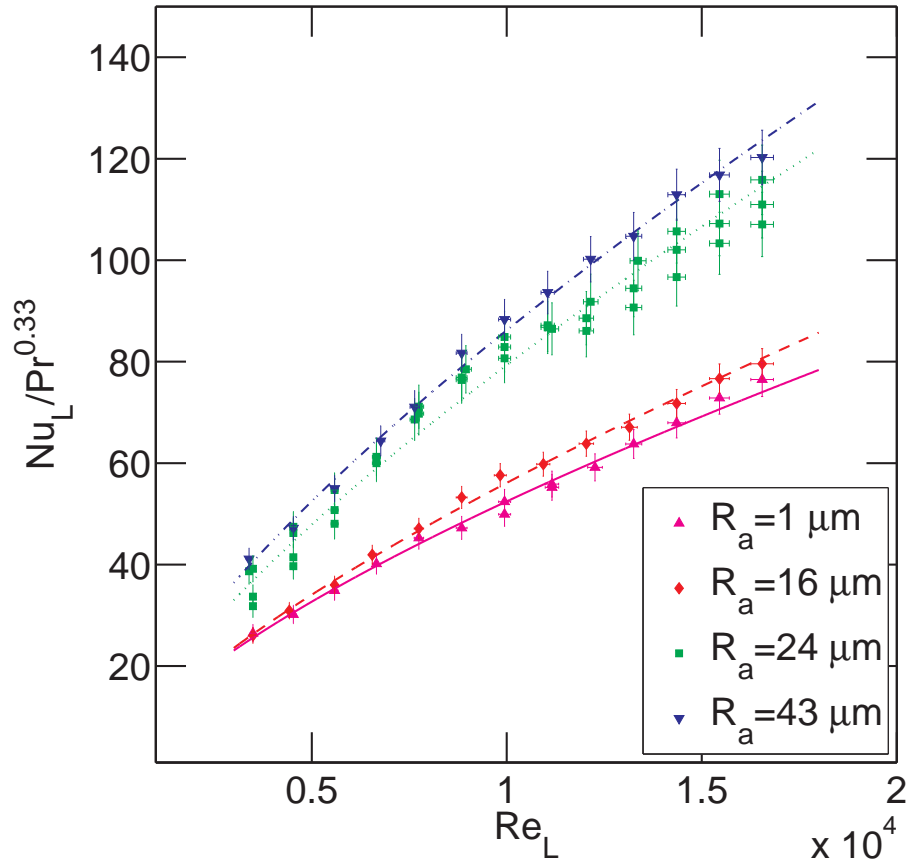
32

Figure 8: Experimental data about convective heat transfer (sample #1, #2 and #3, see Fig. 2). Smooth sample ($R_a \approx 1~\mu m$) with the identical geometry was used as reference. See the Appendix A for experimental uncertainties.

Table 4: Experimental data about convective heat transfer for the flat reference ($R_a \approx 1$ μm, smooth).

v	Re_L	T_s	T_a	V^2/R_h	h	$Nu_L/Pr^{1/3}$	σ_h
$[m/s]$		$[K]$	$[K]$	$[W]$	$[W/m^2 K]$		$[\%]$
3.4	$3.49{\times}10^3$	335.0	302.4	0.1271	30.80	26.47	6.55
4.4	$4.53{\times}10^3$	331.0	302.2	0.1271	35.10	30.17	5.97
5.4	$5.58{\times}10^3$	327.2	302.2	0.1270	40.58	34.88	5.48
6.4	$6.66{\times}10^3$	324.2	302.5	0.1270	46.75	40.17	5.14
7.4	$7.75{\times}10^3$	321.2	301.9	0.1270	52.67	45.27	4.88
8.4	$8.84{\times}10^3$	319.9	301.4	0.1270	54.95	47.23	4.79
9.4	$9.94{\times}10^3$	318.2	300.7	0.1269	58.08	49.91	4.69
9.4	$9.94{\times}10^3$	317.2	300.4	0.1275	60.96	52.39	4.65
10.5	$1.12{\times}10^4$	316.4	300.4	0.1274	64.24	55.21	4.59
10.5	$1.12{\times}10^4$	316.5	300.8	0.1273	65.00	55.86	4.58
11.5	$1.23{\times}10^4$	315.3	300.4	0.1274	68.85	59.17	4.52
12.4	$1.33{\times}10^4$	314.3	300.4	0.1273	74.19	63.76	4.46
13.4	$1.44{\times}10^4$	313.3	300.3	0.1273	79.07	67.96	4.42
14.4	$1.55{\times}10^4$	312.5	300.4	0.1273	84.75	72.83	4.38
15.4	$1.65{\times}10^4$	312.0	300.5	0.1274	88.97	76.47	4.36

Table 5: Experimental data about convective heat transfer for the sample #3 ($R_a = 43$ μm, maximum roughness).

v	Re_L	T_s	T_a	V^2/R_h	h	$Nu_L/Pr^{1/3}$	σ_h	E
$[m/s]$		$[K]$	$[K]$	$[W]$	$[W/m^2 K]$		$[\%]$	$[\%]$
3.3	3.39×10^3	324.2	303.5	0.1293	47.82	41.10	5.21	55.3
4.4	4.53×10^3	321.7	303.5	0.1293	54.87	47.16	4.96	56.3
5.4	5.58×10^3	319.2	303.5	0.1292	63.98	54.98	4.78	57.7
6.5	6.77×10^3	316.7	303.2	0.1290	74.90	64.37	4.65	60.2
7.3	7.64×10^3	315.0	302.8	0.1289	82.66	71.04	4.57	57.0
8.4	8.84×10^3	311.1	300.5	0.1280	95.04	81.68	4.52	73.0
9.4	9.94×10^3	310.4	300.6	0.1276	102.74	88.30	4.49	68.6
10.4	1.10×10^4	309.7	300.4	0.1274	108.93	93.62	4.48	69.6
11.4	1.22×10^4	309.1	300.5	0.1273	116.58	100.19	4.47	69.3
12.4	1.33×10^4	308.7	300.5	0.1268	121.85	104.72	4.47	64.3
13.4	1.44×10^4	308.1	300.4	0.1266	131.37	112.91	4.47	66.2
14.4	1.55×10^4	307.8	300.4	0.1264	135.91	116.80	4.47	60.4
15.4	1.65×10^4	307.6	300.4	0.1262	139.91	120.24	4.47	57.3
						Average		62.7

with higher thermal conductivity (e.g. nylon) present a larger thermal footprint, and this consequently affects the effective characteristic length of the heating edge. However, in the present case, a nylon support was preferred in order to minimize the mounting errors, in spite of a lower agreement with the correlation of Maddox & Mudawar (which could be anyway recovered by redefining a new characteristic length L').

First of all, and more importantly, the rough surfaces made by direct metal laser sintering (DMLS) show an enhanced convective heat transfer. In particular, even though the average roughness R_a is not the best parameter to scale the heat transfer enhancement (see next), as expected the rougher the better. For a more quantitative analysis, the experimental data of the smoothest $R_a \approx 1 \ \mu m$ reference surface are reported in Table 4 and those of the roughest $R_a = 43 \ \mu m$ sample #3 are reported in Table 5. Defining the heat transfer enhancement E as the percentage increase of the rough surface for convective heat transfer with respect to the smoothest reference (assumed representative of milling processes), the sample #3 showed a peak enhancement of 73% and an average of 63%. This is the best result achieved so far during the present activity. This enhancement could not be simply explained in terms of effective area increase, as visible in Table 2. Even though the results are still part of an on-going effort, because many process parameters might be explored, this result would be considered very promising in many engineering applications, including electronics cooling. In electronics cooling, in fact, a few percent of heat transfer enhancement may lead to material saving of heat sinks and hence a significant economical profit, in case of the production of large amounts of standardized products.
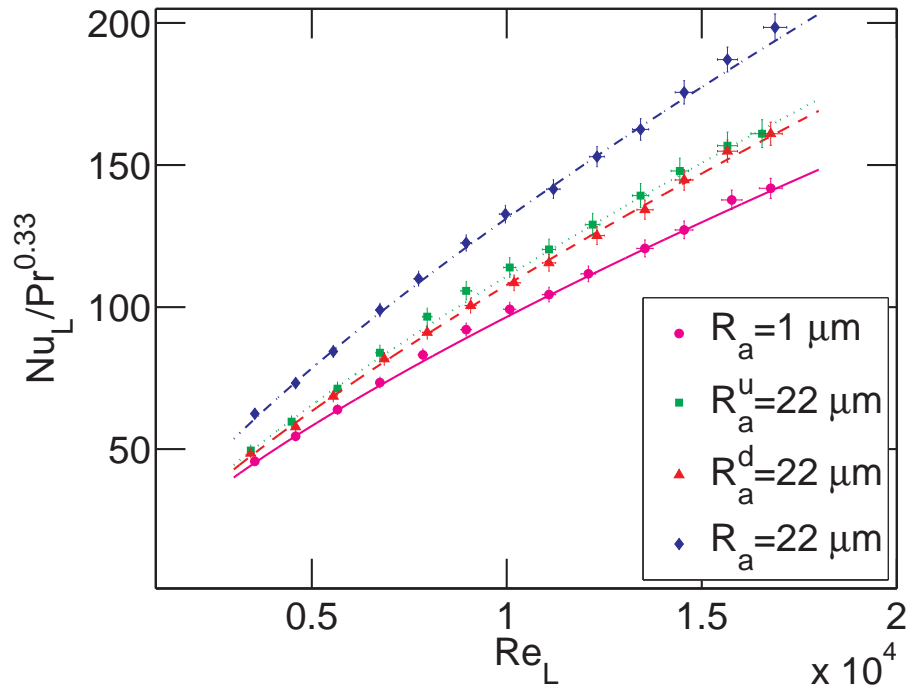
36

Figure 9: Experimental data about convective heat transfer of finned surfaces (sample #4 and #5, see Figs. 2 and 3). Smooth sample ($R_a \approx 1~\mu m$) with the identical geometry was used as reference. R_a^u refers to sample #5 mounted with smooth half fin upstream (vice versa for R_a^d). See the Appendix A for experimental uncertainties.

Table 6: Experimental data about convective heat transfer for the (single) finned reference ($R_a \approx 1\ \mu m$, smooth). For computing the average convective heat transfer coefficient and the Nusselt number, the total finned surface A_f was used.

v [m/s]	Re_L	T_s [K]	T_a [K]	V^2/R_h [W]	h_f [W/m²K]	$Nu_L/Pr^{1/3}$	σ_h [%]
3.4	3.54×10^3	315.2	297.9	0.3605	52.85	45.69	3.38
4.4	4.59×10^3	312.4	297.8	0.3601	63.05	54.52	3.02
5.4	5.66×10^3	310.1	297.5	0.3592	73.92	63.91	2.78
6.4	6.75×10^3	308.3	297.4	0.3591	84.92	73.42	2.64
7.4	7.85×10^3	307.0	297.3	0.3587	96.22	83.20	2.56
8.4	8.96×10^3	306.1	297.4	0.3582	106.49	92.07	2.53
9.4	1.01×10^4	305.7	297.6	0.3580	114.77	99.23	2.51
10.3	1.11×10^4	305.4	297.7	0.3576	120.77	104.41	2.50
11.2	1.21×10^4	305.0	297.7	0.3575	129.20	111.70	2.50
12.5	1.35×10^4	304.5	297.8	0.3570	139.55	120.65	2.50
13.4	1.45×10^4	304.3	297.7	0.3662	147.07	127.16	2.49
14.5	1.58×10^4	303.8	297.8	0.3656	159.28	137.72	2.51
15.4	1.68×10^4	303.6	297.7	0.3653	164.01	141.80	2.52

Table 7: Experimental data about convective heat transfer for the (smoothed tip) sample #4 ($R_a = 22 \ \mu m$, maximum roughness). For computing the average convective heat transfer coefficient and the Nusselt number, the total finned surface A_f was used.

v	Re_L	T_s	T_a	V^2/R_h	h_f	$Nu_L/Pr^{1/3}$	σ_h	E
$[m/s]$		$[K]$	$[K]$	$[W]$	$[W/m^2K]$		$[\%]$	$[\%]$
3.4	3.54×10^3	323.3	304.7	0.5229	72.26	62.48	2.89	36.7
4.4	4.59×10^3	319.3	303.3	0.5251	84.73	73.26	2.68	34.4
5.3	5.55×10^3	318.5	304.6	0.5195	97.58	84.37	2.58	32.0
6.4	6.75×10^3	315.2	303.2	0.5240	114.47	98.97	2.46	34.8
7.3	7.74×10^3	313.9	303.0	0.5233	127.22	109.99	2.42	32.2
8.4	8.96×10^3	313.8	304.0	0.5230	141.75	122.55	2.40	33.1
9.3	9.96×10^3	312.1	303.0	0.5247	153.52	132.73	2.38	33.8
10.4	1.12×10^4	311.6	303.0	0.5243	163.67	141.51	2.38	35.5
11.4	1.23×10^4	311.1	303.1	0.5238	176.88	152.93	2.38	36.9
12.4	1.34×10^4	311.4	304.0	0.5184	187.99	162.54	2.40	34.7
13.4	1.45×10^4	310.0	303.0	0.5235	203.07	175.58	2.41	38.1
14.4	1.57×10^4	309.6	303.1	0.5235	216.42	187.12	2.42	35.9
15.5	1.69×10^4	310.0	303.8	0.5235	229.52	198.44	2.45	39.9
						Average		35.2

In order to prove that the previous enhancements are not limited to flat surfaces only, some experimental tests were performed with (single) finned rough surfaces as well. The experimental data about convective heat transfer of finned surfaces (sample #4 and #5, see Figs. 2 and 3) are reported in Fig. 9, again in terms of the Nusselt number $Nu_L = h_f L / \lambda$ and Re_L. For a more quantitative analysis, the experimental data of the smoothest $R_a \approx 1~\mu m$ finned reference surface are reported in Table 6 and those of the roughest $R_a = 22~\mu m$ sample #4 are reported in Table 7. The heat transfer enhancement is confirmed in this case as well: The sample #4 showed a peak enhancement of 40 % and an average of 35 %. The enhancement is smaller than that the one observed in the case of flat surfaces (roughly half). First, It should be noticed that the roughness parameters for the finned sample #4 are smaller than those of the roughest flat sample #3, as reported in Table 2. Second, the fluid dynamic conditions of the finned sample are completely different than those considered in the previous case: especially the fin tip yields the development of a new velocity boundary layer, superposing with the developing thermal boundary layer.

Further tests were designed to investigate the distribution of convective heat transfer on the latter sample. The fin area is 3/4 the total convective area. By assuming also that convective heat transfer coefficient on the horizontal surfaces of the smooth finned sample is equal to that on the smooth flat sample, it is possible to find out that convective heat transfer coefficient on fin sides is almost twice than that on horizontal surfaces. Hence it is important to investigate particularly the fin sides. The sample #5 (see Fig. 3) was made by milling horizontal surfaces and half of the fin sides of the

previous sample #4. Consequently it was tested once by mounting it with smooth half fin upstream and once downstream (corresponding to R_a^u and R_a^d in Fig. 9). We found that smoothing (upstream) half of the fin sides the convective heat transfer is almost cut by half as well, confirming that most of the heat transfer is due to the fin. However, mounting the same sample #5 in downstream setup, the heat transfer reduction is even larger: This indicates that rough regions of the fin sides are more effective when farther from the leading edge of the boundary layer. The analysis is made even more complex by including transient effects, and further investigations are certainly required in the future in order to optimize the roughness distribution.

The experimental evidences reported in this section are enough to regard DMLS as an interesting technology, in the realm of convective heat transfer augmentation. However, a theoretical explanation is also highly desirable in order to both justify the obtained results and come up with a general tool for future studies and improvements. A theoretical framework, within which the above experimental data could be explained, is reported in the next section.

3. THEORETICAL MODELS

Turbulent flows over rough walls represent a long-standing problem (since 1930s, at the latest), although a lot of work has been already carried out. However, looking at the published literature, the main conclusion is that turbulent structure close to rough walls is far from being fully understood (see, e.g., [46] and references therein). This is the prototypical example of a topic which seems heuristically solved (i.e. many operational formulas exist to design engineering devices involving turbulent flows over rough

walls) but, surprisingly, fundamental understanding is still lacking. Even in classical textbooks (e.g. [47]), it was already pointed out that the number of parameters describing roughness is extraordinarily large owning to the great diversity of geometric forms. It has been suggested that the details of the rough wall may influence the flow across the whole boundary layer, but some care must be taken to sort those claims and their significance in truly understanding wall turbulence [46]. Modern theories do not provide much more than taxonomic classification into wide categories [46], i.e. k-roughness and d-roughness, depending on the existence of significant stagnation on the rough surface. Even when some quantitative parameters seem to be relevant for characterizing wall roughness, as in the case of the equivalent grain size of the Nikuradse's sand [47], typically, it is only a convenient way of characterizing the drag increment due to the roughness [46] and, hence, its effects on turbulent flows. In some scientific communities, a few parameters which are conceptually very different, e.g. frontal solidity and plane solidity, are used interchangeably. Many of the suggested correlations are restricted to surfaces with simple geometry, and cannot easily cope with irregular surfaces [46]. In general, extensive experimental work is currently ongoing to visualize the actual vortices under turbulent boundary layers at rough walls.

Only recently, a pioneering paper by Gioia *et al.* [48] succeeded in explaining the classical Nikuradse's experiment results and in recovering the empirical scaling laws of Blasius and Strickler (on the basis of another classical result, namely the phenomenological theory of Kolmogórov). The basic idea was to estimate the size of the eddies that dominate the momentum transfer close to the wall by a combination of the size of the roughness el-

ements and the viscous length scale. We found this quite enlightening, and thus decided to further extend the idea of Gioia *et al.* (focusing though on convective heat transfer), in order to explain the previous experimental data.

3.1. Sand-based models

Before introducing the sand-based models and, more generally, the theoretical models for roughness, it is worth the effort to clarify which Reynolds number is most suitable for the following analysis. In the previous sections, the Reynolds number based on the heated edge Re_L was used, because the average convective heat transfer coefficient h depends on the heat sink edge L, namely larger L yields to smaller h for the same fluid flow [44, 45]. This is due to the developing thermal boundary layer determined by the heat sink. On the other hand, most of the theoretical models for roughness have been proposed for fully developed thermal flows and they refer to the Reynolds number Re_D based on hydraulic diameter D. Clearly a theoretical model for roughness taking into account also a variable thickness of the thermal boundary layer and its interactions with roughness structures would be preferable. However, to the best of our knowledge, such a model does not exist. Hence we decided to derive the theoretical part by Re_D, to rely on the fitting parameters of the proposed model for including the effects due to developing thermal boundary layer and to compare the theoretical expectations with the experimental data by rescaling them in terms of $Re_L = (L/D)Re_D$.

Coming back to the sand-based models, the pressure gradient inside a pipe can be expressed as a function of the dimensionless friction factor f, namely $\nabla p = (f/D)\rho v^2/2$. In case of smooth pipe turbulent flow, the friction factor can expressed by the phenomenological correlation proposed by Blasius

43

[47], $f_B = f_B(Re_D) = 0.3164\,Re_D^{-1/4}$, where Re_D is the Reynolds number based on the pipe diameter and on the average flow speed. In contrast, for rough pipes, the friction factor depends on the characteristic length-scales of the considered roughness. Clearly, the number of length-scales describing roughness is extraordinarily large owning to the great diversity of geometric forms [47]. However, with the idea of characterizing artificial roughness by a single length-scale only, Nikuradse used circular pipes with their internal walls fully covered with sand of definite grain size (particle diameter) k_s [47]. Systematic and accurate measurements lead to the following single-scale correlation for the friction factor:

$$f_N = f_N(Re_D,\, k_s/R), \qquad (8)$$

where $R = D/2$ is the pipe radius, while the Blausius correlation is recovered for $f_N(Re_D, k_s/R \to 0) = f_B(Re_D)$. The friction factor affects the convective heat transfer, as it is well known by the Reynolds's analogy [47]. For instance, considering the phenomenological correlation proposed by Gnielinsky [49] which rules the convective heat transfer for turbulent flows within pipes, the Nusselt number Nu_D (based on the pipe diameter) reads: $Nu_D = Nu_D(Re_D,\, k_s/R)$. The convective heat transfer enhancement due to roughness can be defined as

$$E = \frac{Nu_D(Re_D,\, k_s/R) - Nu_D(Re_D, 0)}{Nu_D(Re_D, 0)} = E(Re_D,\, k_s/R). \qquad (9)$$

In order to recast the above formula (9) in more explicit terms, let us consider the simplified model presented in Ref. [48], where the Nikuradse's experiments were modeled by the phenomenological theory of Kolmogórov. In particular, let us neglect the correction for the energetic range of the

turbulence spectrum (i.e. $\gamma = 0$). This model is sufficiently accurate to explain the dissipative and the inertial regimes, which are believed to be the two most relevant regimes close to the wall, where roughness plays a dominant role. According to such a model

$$f_G = K\,\sigma^{1/3}\sqrt{\left(\frac{\delta}{\sigma}\right)^{2/3}\Gamma_{-2/3}\left(\frac{\delta}{\sigma}\right)}, \tag{10}$$

where $\sigma = k_s/R + a\,\eta/R$ is the size of the largest eddy that fits the coves between successive roughness elements, $\eta/R = b\,Re_D^{-3/4}$ is the size of the Kolmogórov smallest eddies, $\delta = \beta\,\eta/R$ is the dissipative scale, $\Gamma_{-2/3}$ is the gamma function extended to order $-2/3$ and K is a proper constant ($a = 5$, $b = 11.4$, $\beta = 2.1$ and $K = 0.015$ in Ref. [48]). The inertial regime is defined by $k_s \gg a\,\eta$ (and $\delta/\sigma \to 0$), the dissipative regime by $k_s \sim a\,\eta$ and, finally, the almost-smooth regime by $k_s \ll a\,\eta$ (and $\delta/\sigma \to \beta/a$). In order to proceed further, we will use the Reynolds analogy (see [1] and Colburn's relation therein) for linking the friction factor with the convective heat transfer, namely $Nu_D \propto f_G$. The Reynolds analogy was derived under strong simplifying assumptions, which may not be applicable to any rough surface with any possible morphology. However this represents a first step, which requires further experimental verification. Using Eq. (10) for computing the friction factor, assuming $Nu_D \propto f_G$ and substituting Nu_D into into Eq. (9), it is possible to derive the theoretical enhancement E according to the model presented in Ref. [48], namely

$$E = \frac{f_G(Re_D,\,k_s/R) - f_G(Re_D,0)}{f_G(Re_D,0)}. \tag{11}$$

Before proceeding further, it is convenient to introduce the aerothermal

efficiency η_A, defined as

$$\eta_A = \frac{Nu_D(Re_D, \, k_s/R)/Nu_D(Re_D, \, 0)}{[f_G(Re_D, \, k_s/R)/f_G(Re_D, \, 0)]^{1/3}}. \tag{12}$$

The aerothermal efficiency expresses how much heat transfer enhancement can be achieved by a given pressure loss and it can be used to find optimal solutions in practical devices [50]. In our case, assuming valid the Reynolds analogy, η_A can be expressed by means of the heat transfer enhancement E, namely $E = \eta_A^{3/2} - 1$ or equivalently $\eta_A = (1 + E)^{2/3}$. Hence, the pressure drops will not be discussed explicitly in the following and we will focus on E only.

It is useful to link the above quantity E with the shear stress due to roughness. The shear stress at the wall of a pipe τ is related to the pressure gradient inside the pipe ∇p by the linear relation $\tau = \nabla p \, D/4$, where D is the pipe diameter. Combining the previous relations yields $\tau = (f/8) \, \rho \, v^2/2$. The shear stress can be used to define the friction velocity v_*, namely $v_* = \sqrt{\tau/\rho} = v \, \sqrt{f/8}$, and, consequently, the friction length $y_0 = \nu/v_*$, where ν is the kinematic viscosity of the fluid. The friction length y_0 is useful to define a dimensionless distance from the wall, $y^+ = y/y_0$ (with y being the distance from the wall) and to formulate the following logarithmic law due to Von Kármán, $v^+ = v/v_* = \kappa^{-1} \ln y^+ + A$, where κ is the Von Kármán's constant and A is a constant for smooth walls (see below for rough surfaces). Assuming $f \propto Nu_D$, the friction length can be expressed as a function of the heat transfer enhancement, namely

$$y_0 = \frac{D}{Re_D \, \sqrt{f/8}} = \frac{D}{Re_D \, \sqrt{f_B/8 \, (1 + E)}} \approx \frac{5D}{Re_D^{7/8} \, \sqrt{1 + E}}. \tag{13}$$

46

The previous quantity allows one to normalize the roughness height k_s by the friction length y_0, namely $k_s^+ = k_s/y_0$, as it is done in the following sections.

To summarize, the sand-based model is given by Eqs. (11). The model predicts the heat transfer enhancement as an increasing function of Re_D and k_s/R (or equivalently k_s^+). This model, though, has the serious limitation to characterize the roughness by only one parameter, namely k_s/R, relying upon some morphological constraints (as in the Nikuradse's experiments). Even though this is consistent with Nikuradse's data, it is not always applicable to complex multi-scale roughness, where multiple geometrical features emerge. This limitation will be addressed in the sections below, where more sophisticated models are presented.

3.2. Canopy-based models

In the previous section, a simple model to take into account the role of roughness on heat transfer was derived. However some problems remain. First of all, the roughness obtained by Nikuradse with sand can be said to be of maximum density. In several applications, though, the density of the roughness elements on the wall is considerably smaller and the role of roughness can no longer be described by a single geometrical parameter. This problem was already recognized long time ago. Schlichting introduced the notion of equivalent sand roughness [47], defined as the (fictitious) value of k_s generating the same pressure drops as the actual rough surface in case of high Reynolds numbers. Unfortunately this parameter depends indirectly on the surface morphology and it can be estimated only by experiments. Schlichting [47] investigated artificial roughness made by sparse structures, but the equivalent sand roughness k_s has no evident dependence on the geo-

metrical features of the structures. For example, he considered some rows of spheres with diameter k_p (representative of the protrusion peaks) at distance L_p each other. For $L_p/k_p = 2.44$, he found that the equivalent sand roughness is $k_s/k_p = 3.1$, for $L_p/k_p = 1.46$ he found $k_s/k_p = 3.8$ and, finally, for the densest arrangement (L_p/k_p not reported) he found $k_s/k_p = 0.6$, i.e. $k_s < k_p$ [47]. For this reason, from the practical point of view, Moody performed extensive experiments in order to characterize commercial rough pipes, without any ambition to provide a complete theoretical explanation [47].

The basic problem is that a single geometrical parameter is not enough to fully characterize complex surface morphologies. Higher order statistical moments should be considered or, at least, a parameter for describing the sparsity of roughness peaks. Here a very simple model is proposed to elucidate this concept. In atmospheric science and environmental engineering, many attempts have been made in order to investigate the passive scalar transport within idealized regular structures at the wall, often called model plant canopy [51, 52, 53]. Those studies have been already successfully applied to study the aerodynamic properties of urban areas [54], which still represents an intensive research field [55]. Canopy models typically describe the velocity profile on rough surfaces by the classical semi-logarithmic profile [56], namely

$$v^+ = \frac{1}{\kappa} \ln \left(\frac{y - z_d}{z_o} \right), \tag{14}$$

where κ is the Von Kármán constant being typically 0.41, z_d is called displacement and z_o is the aerodynamic roughness length. The latter quantity can be computed by means of correlations, such as

$$\frac{z_0}{k_p} = \alpha_1 \, \lambda_p \left[\exp \left(\alpha_2 - \alpha_2 \, \lambda_p \right) - 1 \right], \tag{15}$$

where λ_p is the roughness plan aspect ratio [54] (also named plane solidity in mechanical engineering), $\alpha_1 = 0.1$ and $\alpha_2 = 2.44$ (fitting based on Fig. 1 in Ref. [54]). It is also common to report z_0 as a function of the frontal aspect ratio λ_f [54], but the latter is more difficult to be computed as statistical moment of the roughness peaks distribution (as done below). We assume for a double length-scale model that λ_p can be computed as

$$\lambda_p = \frac{k_a}{k_p} = \frac{1}{k_p\,S} \int_S \mathcal{R}(z)\,dS, \tag{16}$$

S is the rough surface, z is the height of the generic rough surface point with regards to the fluid dynamic reference plane, $k_p = \max\left[\mathcal{R}(z)\right]$, $\mathcal{R}(x)$ is the ramp function, namely $\mathcal{R}(x) = x\,\mathcal{H}(x)$, and $\mathcal{H}(x)$ is the Heaviside step function. With other words, the ramp function is $\mathcal{R}(x) = x$ for $x \geq 0$ and zero otherwise, meaning that the ramp function allows one to take into account only positive values. The previous definition of λ_p is consistent with the morphometric analysis of the idealized roughness made of separate blocks (see, e.g., Fig. 2 in Ref. [54]). An alternative approach to generalize λ_p is reported in the Appendix B.

In the industrial context, the velocity profile on rough surfaces is often expressed as [47]

$$v^+ = \frac{1}{\kappa} \ln\left(\frac{y}{k_s}\right) + B(k_s^+) = \frac{1}{\kappa} \ln\left[\frac{y}{k_s} \exp\left(\kappa\,B\right)\right], \tag{17}$$

where $B = B(k_s^+)$ is a universal function, valid for any roughness. Assuming $y \gg z_d$ and matching Eq. (14) with Eq. (17) yields

$$z_0^+ = k_s^+ \exp\left[-\kappa\,B(k_s^+)\right]. \tag{18}$$

49

Eq. (18) establishes a correlation between z_0^+ and k_s^+. In the laminar region, i.e. $k_s^+ \leq a$ [48], Eq. (17) should match the following

$$v^+ = \frac{v}{v_*} = \frac{1}{\kappa} \ln y^+ + A, \tag{19}$$

where $A \approx 5.1$. Hence, $B_{k_s^+ \leq a} = A + 1/\kappa \ln k_s^+$ and substituting into Eq. (18) yields $z_0^+|_{k_s^+ \leq a} = \exp(-\kappa A)$. In the laminar region $y_0/R = 10\, Re_D^{-7/8}$, see Eq. (13), then laminar flow is established if $z_0/R \leq 10 \exp(-\kappa A)\, Re_D^{-7/8}$. Otherwise, for $z_0/R > 10 \exp(-\kappa A)\, Re_D^{-7/8}$, we consider $k_s \sim a\,\eta$, which corresponds to the minimum friction factor for a given roughness k_s/R (see Fig. 4 of Ref. [48]) and to the maximum value of $B(k_s^+)$, namely $B_{k_s \sim a\eta} = B_{max} \,(\approx 9.5)$ [47]. Consequently $z_0^+|_{k_s \sim a\eta} = k_s^+ \exp(-\kappa B_{max})$ and $k_s/R = (z_0/R) \exp(\kappa B_{max})$. Taking into account the previous two limiting cases (namely $k_s^+ \leq a$ and $k_s^+ \sim a\,\eta^+$), a piecewise approximation of Eq. (18) is given by

$$\left(\frac{k_s}{z_0}\right)' = \exp(\kappa B_{max})\, \mathcal{H}\left[z_0/R - 10 \exp(-\kappa A)\, Re_D^{-7/8}\right]. \tag{20}$$

Better approximations could be found by solving the implicit condition given by Eq. (18). For example, for the range of parameters under investigation in the present work, a reasonable heuristic fitting is given by

$$\frac{k_s}{z_0} = \left(\frac{k_s}{z_0}\right)' \left(\frac{z_0/R}{z_\alpha/R}\right)^{-1/5} \left(\frac{Re_D}{Re_\alpha}\right)^{-1/6}, \tag{21}$$

where $z_\alpha/R = 2.642 \times 10^{-4}$ and $Re_\alpha = 50,000$ are optimal fitting parameters.

To summarize, the canopy-based model is based on the following algorithm: the roughness plan aspect ratio is first evaluated by Eq. (16); subsequently, we compute the ratio between aerodynamic roughness length and

peak height z_0/k_p by Eq. (15), k_s/z_0 by Eq. (21) at a given Re_D, and the relative roughness by

$$\frac{k_s}{R} = \frac{k_p}{R}\frac{z_0}{k_p}\frac{k_s}{z_0}.$$ (22)

Finally, an estimate of the heat transfer enhancement is obtained by Eq. (11), in terms of $E = E(k_s/R, Re_D)$. The canopy-based model depends on both the roughness peak k_p and the average peak height k_a (because $\lambda_p = k_a/k_p$). Even though this is a clear improvement towards a multi-scale (i.e. multi-parameter) description, this model still predicts a fixed parameter to characterize the surface roughness, namely k_s/R. This assumption can be relaxed by the following model, as also confirmed by our experimental evidences.

3.3. Proposed model

Similarly to Ref. [48], the key idea is again to estimate the size of the eddies that dominate the heat transfer close to the wall by a combination of the size of the roughness elements, i.e. k_p and k_a, and the viscous length scale η. In this way, the fluid dynamic roughness is not a mere geometrical factor but it depends also on the turbulent fluid flow. This is consistent with other modeling practices in environmental engineering, where the aerodynamic roughness length z_0 has been proposed [56]. Usually two length-scales compete: laminar dissipative structures ruled by η, and roughness dominated features ruled by k_a and/or k_p. Clearly, the latter is a simplified vision due to the presence of a full range of intermediate scales in actual flows. In particular, at low Reynolds numbers, it is reasonable to imagine that fluid dynamic structures depending on both η and k_p are present (at low Reynolds numbers, k_p is more likely than k_a because peaks emerge first from the viscous
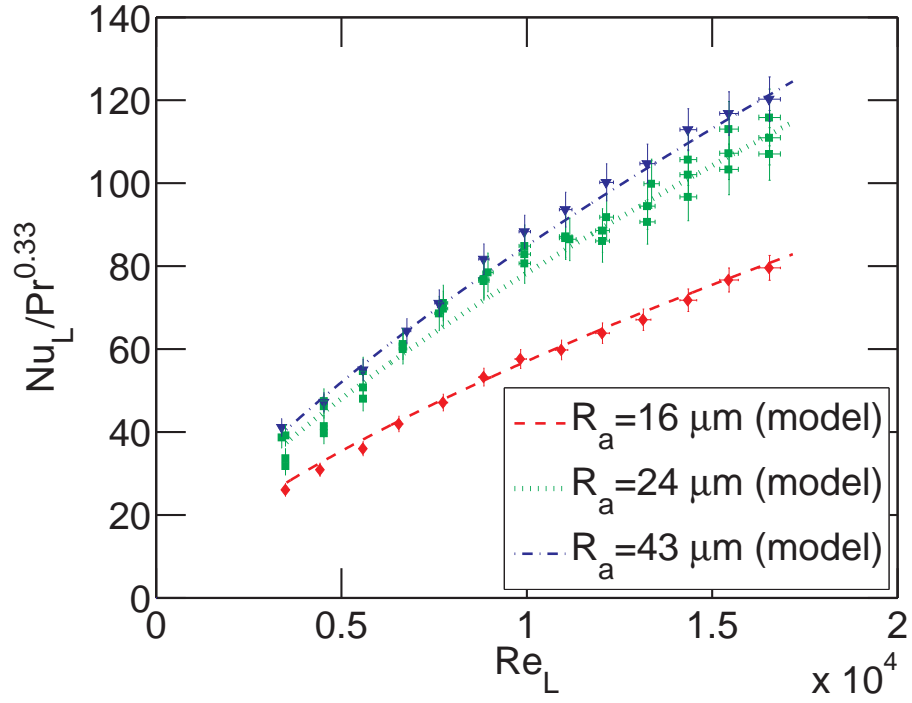
Figure 10: Comparison between the proposed theoretical model and the experimental data about convective heat transfer. The experimental data and the meaning of the point marks are the same of Fig. 8. See the Appendix A for experimental uncertainties. Lines correspond to the proposed model for different values of average roughness R_a. Even though the proposed model was formulated in terms of Re_D, the present plot is reported in terms of Re_L, where $Re_L = (L/D) Re_D$.

sublayer). However, the bottom part of roughness is usually extremely dense, and it likely plays an unessential role in perturbing the boundary layer (see Fig. 6). For this reason, we summarize the geometrical features of roughness in $k_p - k_0$, where k_0 is a shifting parameter of the proposed model. Let us suppose that, in the regime between smooth flows (dominated by η) and fully rough flows (dominated by k_p or better $k_p - k_0$), intermediate-Reynolds structures have a volume proportional to $\sim \eta^2 (k_p - k_0)$, like these structures are attached to rough protrusions $k_p - k_0$ (orthogonal to to the wall) but they are still stable enough to have plan area of η^2. A possible length scale would be $\sim \sqrt[3]{\eta^2 (k_p - k_0)}$. Taking into account that $\eta/R = b \, Re_D^{-3/4}$ yields

$$\frac{k_p^{eff}}{R} = c \, Re_D^{-1/2} \sqrt[3]{\frac{k_p - k_0}{R}}, \tag{23}$$

where c is a tunable constant of the proposed model. Eq. (23) is an important theoretical contribution of the present work.

To summarize, the proposed model differs from the previous because the relative roughness is computed as

$$\frac{k_s^{eff}}{R} = \frac{k_p^{eff}}{R} \frac{z_0}{k_p} \frac{k_s}{z_0}, \tag{24}$$

where k_p^{eff}/R is computed by Eq. (23). An estimate of the heat transfer enhancement is given by Eq. (11),

$$E = E\left(Re_D, \, k_s^{eff}/R\right). \tag{25}$$

The proposed model depends on both geometrical parameters, i.e. k_a and k_p, as well a fluid dynamic parameter, i.e. η, by means of an intermediate
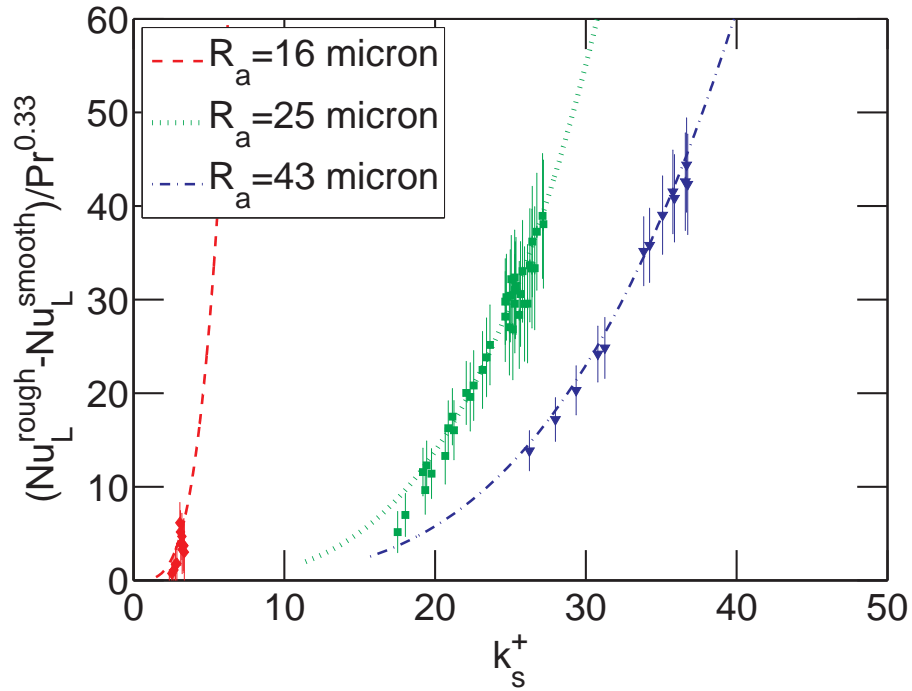
Figure 11: Comparison between the proposed theoretical model and the experimental data about convective heat transfer. The experimental data and the meaning of the point marks are the same of Fig. 8. See the Appendix A for experimental uncertainties. Increase in terms of the Nusselt number as a function of k_s^+ predicted by the proposed model (dashed lines) and measured by the sensor in Section 2.3 (symbols).

scale $\sqrt[3]{\eta^2 (k_p - k_0)}$. In particular, the latter parameter is not fixed for a given surface but it depends on the turbulent flow as well.

In the following, we used $k_0/R = 1/517$ because this corresponds to the smallest sand roughness considered by Nikuradse. In order to take into account the peculiarities of the DMLS roughness, setting the tunable parameters $c = 5.5$, an excellent agreement is found between the proposed model and the experimental data discussed in the previous section, as shown in Figs. 10 and 11. These fitting parameters are also useful to take into account the effects due to developing thermal boundary layer and its interactions with the roughness structures. In the latter figures, the theoretical expectations due to the proposed model, derived in terms of Re_D in the previous equations, were rescaled by $Re_L = (L/D)Re_D$ in order to compare them with our experimental data.

It is worth the effort to compare our experimental data with other passive heat transfer enhancement techniques. In Figure 12, the relative heat transfer enhancement (with regards to $E_{Re_D=30,000}$) as a function of the Reynolds number is reported. The theoretical model based on the third scale given by Eq. (23) is compared to Gnielinski correlation [49] (friction factors are computed by Moody chart [47] with $e/D = 0.02$ and $e/D = 0.05$, where e is the mean height of roughness of commercial pipes [47]) and other experimental works about passive heat transfer enhancement techniques [57, 58, 59, 60]. As highlighted by this figure, the enhancements due to DMLS samples scale as $E \sim Re_D^{0.07}$, which is perfectly within the expectations based on the scattered literature about passive heat transfer enhancement techniques. In particular, DMLS samples scale less than commercial pipes having $E \sim Re_D^{0.41}$ [49], seem
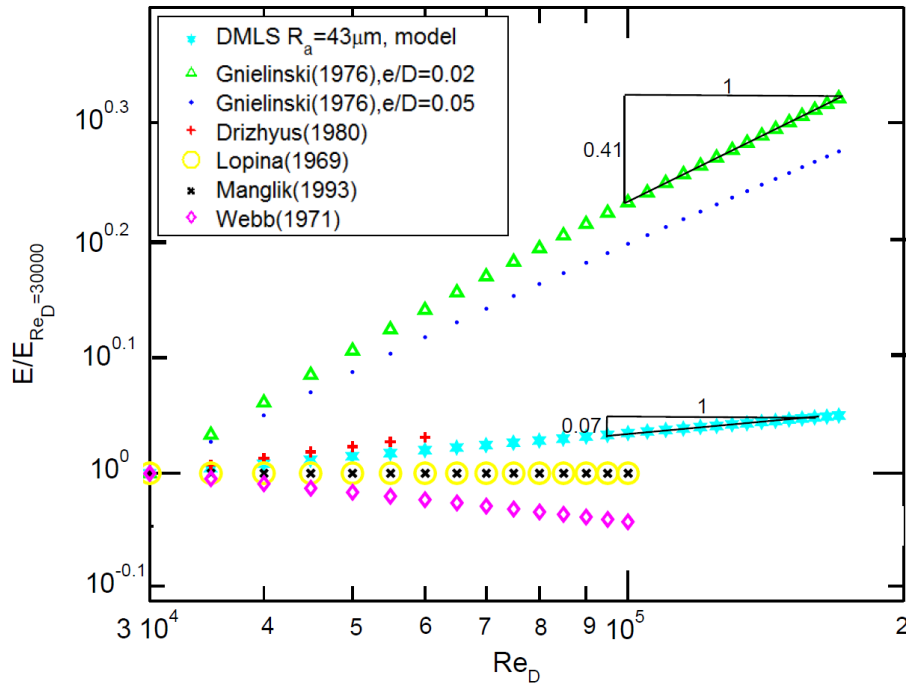
Figure 12: Relative heat transfer enhancement (with regards to $E_{Re_D=30,000}$) as a function of the Reynolds number. The theoretical model based on the third scale given by Eq. (23) is compared with the Gnielinski correlation [49] (with friction factors computed by Moody chart [47]) and other experimental works about passive heat transfer enhancement techniques [57, 58, 59, 60].

56

to achieve among the best performance of twisted tapes [57, 58, 59] and seem to scale more favorably than surfaces with repeated ribs [60].

The experimental results are part of an on-going effort. Consequently they do not allow us to determine univocally the empirical parameters of the proposed model and to evaluate its applicability to other passive heat transfer enhancement techniques. Hence, even though a strong theoretical validation of the model is not fully suitable at this stage, still the proposed third scale given by Eq. (23) is very promising and it would be interesting to generalize it for different morphologies.

4. Conclusions and perspectives

In this paper, for the first time to our knowledge, we experimentally investigate the potential of the DMLS artificial roughness, optimized for convective heat transfer enhancement, in manufacturing flat and finned heat sinks for electronics cooling. For rough flat surfaces, we found a peak of convective heat transfer enhancement of 73% (63% on average), while, for rough (single) finned surfaces, we found a peak enhancement of 40% (35% on average). Data were obtained using a purposely developed novel sensor with maximum and mean estimated tolerance intervals of $\pm 7.0\%$ and $\pm 5.4\%$, respectively. Owing to a huge space of process parameters to be explored, the present work can be regarded as a first (but essential) step aiming at unveiling the great potential of DMLS in electronics cooling. Moreover, the presented results can be easily extended to other industrial sectors involving turbulent flows over walls.

The observed heat transfer enhancement values could not be explained

by the increases of the effective roughness surface area, which was found to be always much smaller (see Table 2). Even though it is known to be a quite old problem, there is no universally accepted theory that can accurately describe turbulent flows in the presence of complex multi-scale roughness (see also [46]). Here, following the idea proposed by the pioneering paper of Gioia *et al.* [48], we elaborated a novel model which we found in excellent agreement with our experimental data. Such a finding looks promising towards a systematic theory of turbulent flows over rough walls, particularly with regards to convective heat transfer.

Acknowledgments

Appendix A. Estimating experimental uncertainties

For statistical analysis reported here and in the main text, a significant level $\alpha = 0.05$ (5%) was adopted. The uncertainties of measurements are divided into two main categories [61]: type A and type B, according to whether they are evaluated by statistical methods or otherwise, respectively. In the

latter category, we included all the information coming from either instruments data sheets or instruments calibrations. Eq. (2) allows one to compute h as a function of other measurements $(V, T_s, T_{g1}, T_{g2}, T_a, T_w)$ and parameters (R_h, ϵ), namely $h = h(V, T_s, T_{g1}, T_{g2}, T_a, T_w; R_h, \epsilon)$. These independent quantities can be organized in a vector, namely $\boldsymbol{q} := \{V, T_s, T_{g1}, T_{g2}, T_a, T_w; R_h, \epsilon\}$, and $q_i \in \boldsymbol{q}$ is the generic i-th quantity. The standard uncertainty $\Sigma_{h,B}$ can be computed by the uncertainty estimation method [61] as

$$\Sigma_{h,B} = \sqrt{\sum_{i=1}^{8} \left(\Sigma_{q_i} \frac{\partial h}{\partial q_i}\right)^2}, \tag{A.1}$$

where Σ_{q_i} is the standard uncertainty for the quantity q_i. Since we are dealing with convective heat transfer due to forced air, the expected thermal powers on a small surface are small as well. Hence, the heating power in Eq. (2) is based on the measured potential difference V only, namely V^2/R_h. The standard uncertainty can be assumed $\Sigma_V = 0.0016$ V according to the producer data sheet. The temperature values T_s, T_{g1}, T_{g2} and T_a are critical and, therefore, thermocouples calibrated by primary standard (ACCREDIA) were used. In order to be on the safe side, the corresponding uncertainties can be assumed equal to $\Sigma_{T_s} = \Sigma_{T_{g1}} = \Sigma_{T_{g2}} = \Sigma_{T_a} = 0.05$ K. On the other hand, the remaining thermocouple might be characterized by $\Sigma_{T_w} = 0.4$ K, because of the intrinsic uncertainties of the installation setup. We measured directly the sample heater resistance, which was equal to 25.6 Ω at room temperature (slight changes of resistivity with regards to ambient temperature were taken into account) and with uncertainty of $\Sigma_{R_h} = 0.014$ Ω. The surface emissivity of samples ϵ was estimated by the procedure described in the main text: The results are reported in Table 3. Considering the difficulties associated with

optical calibrations, we decided to assume a quite large value of uncertainty, i.e. $\Sigma_\epsilon = 0.2$. Using all these values of standard uncertainties Σ_{q_i} and taking into account the experimental results, Eq. (A.1) allowed us to compute $\Sigma_{h,B}$. It proves more convenient to express the uncertainty as a relative quantity, as done in the main text. Hence, we used a power-law least squares fitting, namely $h_F = h_F(v) = d_1 \, v^{d_2}$, where d_1 and d_2 are proper fitting parameters. Consequently the relative B-type uncertainty becomes $\sigma_{h,B} = \Sigma_{h,B}/h_F$.

Let us now focus on the A-type uncertainty. In this work, we propose a novel methodology for convective heat transfer, aiming at (a) evaluating tolerance intervals instead of confidence intervals (because the former are stricter than the latter) and (b) taking advantage of measurements performed at different velocities. First of all, we normalize the convective heat transfer coefficients h_i obtained by n measurements, performed at velocities v_i, with regards to the power-law fitting, namely $h'_i = h_i/h_F(v_i)$. Next we compute the mean value μ' and the standard deviation σ' of the statistical sample made of elements h'_i. We estimate the population mean μ and the maximum population standard deviation σ by the Student's t-distribution and the Chi-squared distribution, respectively. In particular, $\mu = \mu' \pm \sigma_\mu$, where $\sigma_\mu = t_{1-\alpha/2,\,n-1}\,\sigma'/\sqrt{n}$ and $\sigma = \sigma'/\chi_{\alpha/2}\,\sqrt{n-1}$ [61]. The previous standard deviations can be combined as follow

$$\sigma_{h,A} = \sigma' \sqrt{\frac{t^2_{1-\alpha/2,\,n-1}}{n} + \frac{n-1}{\chi^2_{\alpha/2}}}. \tag{A.2}$$

Finally, the relative uncertainty can be obtained as

$$\sigma_h = \sqrt{\sigma^2_{h,A} + \sigma^2_{h,B}}. \tag{A.3}$$

In the reported experimental campaign, the A-type uncertainty was larger than B-type uncertainty (the latter being $\pm 2\%$), as it should be in a properly calibrated measurement equipment. The maximum and mean estimated relative uncertainty σ_h for all the convective heat transfer coefficients is $\pm 7.0\%$ and $\pm 5.4\%$, respectively. It is important to highlight once more that these values are tolerance intervals which are larger than confidence intervals, which are instead usually reported in literature for convective heat transfer measurements (i.e. we preferred to provide more conservative estimates).

Appendix B. Roughness distribution function

There are many different ways to generalize the concept of λ_p used in Ref. [54]. In addition to the one proposed in the main text, here we discuss a further example based on statistical mechanics. According to this approach, the quantity λ_p in Eq. (16) can be interpreted as a truncated first-order statistical moment of a probability density function. Let us introduce $dS|_z$ as the total area characterized by the same height z with regards to the fluid dynamic reference plane. Consequently $dS|_z/S$ can be used to express the probability $dP(z)$ of finding surface at the height z, namely $dP(z) = dS|_z/S$. Hence, it is possible to introduce a probability density function $f(z)$ such that $f(z) = dP(z)/dz$. Consequently Eq. (16) can be rewritten as

$$\lambda_p = \frac{1}{k_p} \int_S \mathcal{R}(z) \frac{dS}{S} = \frac{1}{k_p} \int_{P(k_p)}^{P(0)} z \, dP = \frac{1}{k_p} \int_0^\infty z \, f(z) \, dz, \qquad \text{(B.1)}$$

which proves that λ_p is indeed a truncated first-order statistical moment of $f(z)$. Let us consider again the idealized roughness made of separate blocks, which is used as canopy model in Fig. 2 of Ref. [54]. For the latter block-

based model, it is easy to prove that the probability density function f_C is given by

$$f_C(z) = 2\left(1 - \frac{k_a}{k_p}\right)\delta(z) + \frac{k_a}{k_p}\delta(z - k_p), \qquad \text{(B.2)}$$

where $\delta(z)$ is the Dirac delta function.

[1] A. Bejan and A.D. Kraus (Editors), Heat Transfer Handbook, John Wiley, Hoboken (2003).

[2] J. Sergent and A. Krum, Thermal management handbook for electronic assemblies, McGraw-Hill, New York (1998).

[3] R. Remsburg, Advanced Thermal Design of Electronic Equipment, Chapman & Hall, New York (1998).

[4] S.V. Garimella, A.S. Fleischer, J.Y. Murthy, A. Keshavarzi, R. Prasher, C. Patel, S.H. Bhavnani, R. Venkatasubramanian, R. Mahajan, Y. Joshi, B. Sammakia, B.A. Myers, L. Chorosinski, M. Baelmans, P. Sathyamurthy and P.E. Raad, Thermal Challenges in Next-Generation Electronic Systems, IEEE Transactions on Components and Packaging Technologies 31:4 (2008) 801-815.

[5] P.M. Ligrani, M.M. Oliveira, T. Blaskovich, Comparison of heat transfer augmentation techniques, AIAA Journal 41:3 (2003) 337-362.

[6] J.R. Culham, Y.S. Muzychka, Optimization of plate fin heat sinks using entropy generation minimization, IEEE Transactions on Components and Packaging Technologies 24:2 (2001) 159-165.

[7] C.J. Shih, G.C. Liu, Optimal design methodology of plate-fin heat sinks for electronic cooling using entropy generation strategy, IEEE Transactions on Components and Packaging Technologies 27:3 (2004) 551-559.

[8] W.A. Khan, J.R. Culham, M.M. Yovanovich, The Role of Fin Geometry in Heat Sink Performance, Journal of Electronic Packaging 128:4 (2006) 324-330.

[9] S.W. Chang, T.L. Yang, C.C. Huang, K.F. Chiang, Endwall heat transfer and pressure drop in rectangular channels with attached and detached circular pin-fin array, International Journal of Heat and Mass Transfer 51:21-22 (2008) 5247-5259.

[10] Y.-T. Yang, H.-S. Peng, Numerical study of pin-fin heat sink with uniform fin height design, International Journal of Heat and Mass Transfer 51:19-20 (2008) 4788-4796.

[11] P.M. Ligrani, G.I. Mahmood, J.L. Harrison, C.M. Clayton, D.L. Nelson, Flow structure and local Nusselt number variations in a channel with dimples and protrusions on opposite walls, International Journal of Heat and Mass Transfer 44:23 (2001) 4413-4425.

[12] M.A. Elyyan, A. Rozati, D.K. Tafti, Investigation of dimpled fins for heat transfer enhancement in compact heat exchangers, International Journal of Heat and Mass Transfer 51:11-12 (2008) 2950-2966.

[13] Y. Chen, Y.T. Chew, B.C. Khoo, Enhancement of heat transfer in turbulent channel flow over dimpled surface, International Journal of Heat and Mass Transfer 55:25-26 (2012) 8100-8121.

[14] S.V. Garimella and P.A. Eibeck, Heat transfer characteristics of an array of protruding elements in single phase forced convection, Internal Journal of Heat and Mass Transfer 33:12 (1990) 2659-2669.

[15] G.I. Mahmood, M.Z. Sabbagh, P.M. Ligrani, Heat Transfer in a Channel with Dimples and Protrusions on Opposite Walls, Journal of Thermophysics and Heat Transfer 15:3 (2001) 275-283.

[16] S. Mancin, C. Zilio, A. Diani, L. Rossetto, Air forced convection through metal foams: Experimental results and modeling, International Journal of Heat and Mass Transfer 62:1 (2013) 112-123.

[17] E.K. Kalinin, G.A. Dreitser, Heat Transfer Enhancement in Heat Exchangers, Advances in Heat Transfer 31:C (1998) 159-332.

[18] J.S. Park, J.C. Han, Y. Huang, S. Ou, R.J. Boyle, Heat transfer performance comparisons of five different rectangular channels with parallel angled ribs, International Journal of Heat and Mass Transfer 35:11 (1992) 2891-2903.

[19] X. Gao, B. Sunden, Heat transfer and pressure drop measurements in rib-roughened rectangular ducts, Experimental Thermal and Fluid Science 24:1-2 (2001) 25-34.

[20] G. Tanda, Heat transfer in rectangular channels with transverse and V-shaped broken ribs, International Journal of Heat and Mass Transfer 47:2 (2004) 229-243.

[21] S.W. Chang, T.-M. Liou, M.H. Lu, Heat transfer of rectangular narrow

channel with two opposite scaleroughened walls, International Journal of Heat and Mass Transfer 48:19-20 (2005) 3921-3931.

[22] S.W. Chang, T.M. Liou, K.F. Chiang, G.F. Hong, Heat transfer and pressure drop in rectangular channel with compound roughness of V-shaped ribs and deepened scales, International Journal of Heat and Mass Transfer 51:3-4 (2008) 457-468.

[23] F. Zhou, G.W. Demoulin, D.J. Geb, I. Catton, Closure for a plane fin heat sink with scale-roughened surfaces for volume averaging theory (VAT) based modeling, International Journal of Heat and Mass Transfer 55:25-26 (2012) 7677-7685.

[24] F. Zhou and I. Catton, Numerical Evaluation of Flow and Heat Transfer in Plate-Pin Fin Heat Sinks with Various Pin Cross-Sections, Numerical Heat Transfer - Part A: Applications 60:2 (2011) 107-128.

[25] C. Wang, Y. Yu, T. Simon, T. Cui and M.T. North, Microfabrication of short pin fins on heat sink surfaces to augment heat transfer performance, Proceedings of 13th InterSociety Conference on Thermal and Thermomechanical Phenomena in Electronic Systems - ITherm, San Diego (2012).

[26] D.B. Go, S.V. Garimella, T.S. Fisher, R.K. Mongia, Ionic winds for locally enhanced cooling, Journal of Applied Physics 102 (2007) 053302.

[27] D.B. Go, R.A. Maturana, T.S. Fisher, S.V. Garimella, Enhancement of external forced convection by ionic wind, International Journal of Heat and Mass Transfer 51 (2008) 6047-6053.

[28] T Wohlers, Additive Manufacturing Advances, Manufacturing Engineering, April (2012) 55-63.

[29] T. Wohlers, T. Caffrey, Additive manufacturing going mainstream, Manufacturing Engineering, June (2013) 67-73.

[30] J.P. Kruth, G. Levy, F. Klocke, T.H.C. Childs, Consolidation phenomena in laser and powder-bed based layered manufacturing, CIRP Annals - Manufacturing Technology 56(2) (2007) 730-759.

[31] M. Wong, I. Owen, C.J. Sutcliffe, A. Puri, Convective heat transfer and pressure losses across novel heat sinks fabricated by Selective Laser Melting, International Journal of Heat and Mass Transfer 52 (2009) 281288.

[32] R. Neugebauer, B. Müller, M. Gebauer and T. Töppel, Additive manufacturing boosts efficiency of heat transfer components, Assembly Automation, 31/4 (2011) 344347.

[33] A. Simchi, Direct laser sintering of metal powders: mechanism, kinetics, and microstructural features, Materials Science and Engineering: A 428 (2006) 148-158.

[34] D. Manfredi, F. Calignano, M. Krishnan, R. Canali, E.P. Ambrosio, E. Atzeni, From Powders to Dense Metal Parts: Characterization of a Commercial AlSiMg Alloy Processed through Direct Metal Laser Sintering, Materials 6 (2013) 856-869.

[35] F. Calignano, D. Manfredi, E. P. Ambrosio, L. Iuliano, P. Fino, Influence of process parameters on surface roughness of aluminum parts produced

by DMLS, The International Journal of Advanced Manufacturing Technology 67 (2013) 2743-2751.

[36] EOS datasheet, EOS Aluminium AlSi10Mg for EOSINT M 270 (2011).

[37] ISO 4287: Geometrical Product Specifications (GPS) – Surface texture: Profile method – Terms, definitions and surface texture parameters (R - $parameters$).

[38] ISO 25178: Geometrical Product Specifications (GPS) – Surface texture: areal (S - $parameters$).

[39] E. Chiavazzo, L. Ventola, F. Calignano, D. Manfredi, P. Asinari, A sensor for direct measurement of small convective heat fluxes: Validation and application to micro-structured surfaces, Experimental Thermal and Fluid Science 55 (2014) 42-53.

[40] H. Czichos, T. Saito and L. Smith (Editors), Handbook of Materials Measurement Methods, Springer (2006).

[41] D.G. Holmberg, C.A. Womeldorf, W.L. Grosshandler, Design and Uncertainty Analysis of a Second-Generation Convective Heat Flux Calibration Facility, Proceedings of American Society of Mechanical Engineers (ASME) Heat Transfer Division, Nashville (2001).

[42] ANSYS FLUENT 12.0/12.1 Documentation, ANSYS, Inc.

[43] G.I Mahmood, P.M Ligrani, Heat transfer in a dimpled channel: Combined influences of aspect ratio, temperature ratio, Reynolds number,

and flow structure, International Journal of Heat and Mass Transfer 45:10 (2002) 2011-2020.

[44] D.E. Maddox and I. Mudawar, Single- and two-phase convective heat transfer from smooth and enhanced microelectronic heat sources in a rectangular channel, Journal of Heat Transfer 111:4 (1989) 1045-1052.

[45] C.P. Tso, G.P. Xu, K.W. Tou, An Experimental Study on Forced Convection Heat Transfer From Flush-Mounted Discrete Heat Sources, Journal of Heat Transfer 121 (1999) 326-332.

[46] J. Jiménez, Turbulent Flows over Rough Walls, Annu. Rev. Fluid Mech. 36 (2004) 173-196.

[47] H. Schlichting, K. Gersten, Boundary-layer theory, Springer, 8th ed., Berlin, 2000.

[48] G. Gioia, P. Chakraborty, Turbulent Friction in Rough Pipes and the Energy Spectrum of the Phenomenological Theory, Phys. Rev. Lett. 96 (2006) 044502.

[49] V. Gnielinski, New equations for heat and mass transfer in turbulent pipe and channel flow, International Chemical Engineering 16 (1976) 359-367.

[50] S.C. Jenkins, B. Weigand, J. von Wolfersdorf, S.O. Neumann, Validation and Analysis of Numerical Results for a Varying Aspect Ratio Two-Pass Internal Cooling Channel, Journal of Heat Transfer 133 (2011) 051701.

[51] M.R. Raupach, P.A. Coppin, B.J. Legg, Experiments on scalar dispersion within a model plant canopy part I: The turbulence structure, Boundary-Layer Meteorology 35:1-2 (1986) 21-52.

[52] P.A. Coppin, M.R. Raupach, B.J. Legg, Experiments on scalar dispersion within a model plant canopy part II: An elevated plane source, Boundary-Layer Meteorology 35:1-2 (1986) 167-191.

[53] B.J. Legg, M.R. Raupach, P.A. Coppin, Experiments on scalar dispersion within a model plant canopy, part III: An elevated line source, Boundary-Layer Meteorology 35:3 (1986) 277-302.

[54] C.S.B. Grimmond, T.R. Oke, Aerodynamic Properties of Urban Areas Derived from Analysis of Surface, Form. J. Appl. Meteor. 38 (1999) 1262-1292.

[55] A.J. Arnfield, Two decades of urban climate research: A review of turbulence, exchanges of energy and water, and the urban heat island, International Journal of Climatology 23:1 (2003) 1-26.

[56] H. Tennekes, J.L. Lumley, A First Course in Turbulence, MIT Press, Cambridge, MA, (1972).

[57] M.R.M. Drizhyus, R.K. Shkema, A.A. Shlanchyauskas, Heat transfer in a twisted stream of water in a tube, International chemical engineering 20:3 (1980) 486-489.

[58] R.F. Lopina and A.E. Bergles, Heat transfer and pressure drop in tape-generated swirl flow of single-phase water, Transactions of the ASME (1969).

[59] R.M. Manglik and A.E. Bergles, Heat transfer and pressure drop correlations for twisted-tape inserts in isothermal tubes: part II - Transition and turbulent flows, Transactions of the ASME 115:4 (1993) 890-896.

[60] R.L. Webb, E.R.G. Eckert and R.J. Goldstein, Heat transfer and friction in tubes with repeated-rib roughness, International Journal of Heat and Mass Transfer, 14 (1971) 601-617.

[61] J. Mandel, The Statistical Analysis of Experimental Data, Dover, New York, (1984).